University of South Florida
Scholar Commons

Graduate Theses and Dissertations | Graduate School

2006

Resonance ultrasonic vibrations (RUV) for crack detection in silicon wafers for solar cells

William Dallas
University of South Florida

Follow this and additional works at: http://scholarcommons.usf.edu/etd

Part of the American Studies Commons

Scholar Commons Citation
Dallas, William, "Resonance ultrasonic vibrations (RUV) for crack detection in silicon wafers for solar cells" (2006). *Graduate Theses and Dissertations.*
http://scholarcommons.usf.edu/etd/2497

This Thesis is brought to you for free and open access by the Graduate School at Scholar Commons. It has been accepted for inclusion in Graduate Theses and Dissertations by an authorized administrator of Scholar Commons. For more information, please contact scholarcommons@usf.edu.

Resonance Ultrasonic Vibrations (RUV) for Crack Detection in Silicon Wafers for Solar Cells

by

William Dallas

A thesis submitted in partial fulfillment
of the requirements for the degree
Master of Science in Electrical Engineering
Department of Electrical Engineering
College of Engineering
University of South Florida

Co-Major Professor: Rudiger Schlaf, Ph.D.
Co-Major Professor: Sergei Ostapenko, Ph.D.
Committee Member: Dan Hess, Ph.D.

Date of Approval:
November 2, 2006

Keywords: photovoltaics, non-destructive, characterization, fracture, defect, renewable energy, processing

© Copyright 2006, William Dallas

Dedication

To my loving wife Marisa for her unwavering support through it all.

Acknowledgements

The work presented in this thesis would not have been possible without the help of many people. Foremost, Dr. Sergei Ostapenko for his guidance and technical expertise. The previous students in the defects lab who initiated this work including Anton Belyaev and Igor Tarasov as well as Oleg Polupan for FEA work. I would also like to thank Maciej Dybiec for his help in writing the crack elongation machine's computer interface as well as maintaining an entertaining atmosphere in the laboratory.

Table of Contents

List of Tables iii

List of Figures iv

Abstract vii

Chapter One: Introduction and Background 1
- 1.1 Defining the Need for Renewable Energies 1
- 1.2 Silicon for Photovoltaic Cells 2
  - 1.2.1 Mono-Crystalline Silicon 4
  - 1.2.2 Polycrystalline Silicon 5
  - 1.2.3 Amorphous Silicon 7
- 1.3 Fracture and Cleavage in Silicon 8
- 1.4 Mechanical Characterization Methods 9
  - 1.4.1 Mechanical Bending Tests 10
  - 1.4.2 Optical Transmission 12
  - 1.4.3 Photoluminescence and Electro-luminescence Imaging 14
  - 1.4.4 Infrared Lock-in Ultrasound Thermography 16
  - 1.4.5 Scanning Acoustic Microscopy 16
  - 1.4.6 Impact Testing 20
- 1.5 Finite Element Analysis 21

Chapter Two: Resonance Ultrasonic Vibration System 24
- 2.1 Development of the RUV System 24
- 2.2 RUV System Upgrades 27
  - 2.2.1 Introduction of Adjustable Wafer Alignment 27
  - 2.2.2 Automatic Loading/Unloading 29
  - 2.2.3 CMP Tip and Elastic Element 31
  - 2.2.4 Periphery Scans 33
- 2.3 Current System Description 34
- 2.4 Sample Description 39

Chapter Three: Experiments and Results 40
- 3.1 RUV Mode Identification 40
- 3.2 RUV Crack Detection 48
  - 3.2.1 Crack Engineering 48
  - 3.2.2 Experimental Crack Detection 49

3.2.3 Cracks on Production Grade Wafers 54
3.3 Crack Elongation Apparatus 56
3.4 Liquid Evaporation Crack Detection Method 58

Chapter Four: Conclusions and Recommendations 60

References 64

List of Tables

Table 1.1	Comparison of Mechanical Characterization Methods.	23
Table 3.1	Experimental (a) and FEA Calculated (b) Resonance Peak Frequencies for 4 Vibration Modes in Si Wafers of Different Sizes.	42

List of Figures

Figure 1.1	Four Different Mechanical Bending Tests.	10
Figure 1.2	Optical Transmission μ-crack Detection Apparatus.	13
Figure 1.3	Diagram of μ-crack Widths and Detection Mechanisms.	13
Figure 1.4	Relative Beam Shape of Acoustic Signal as Emitted from Transducer and Focused Near the Center of the Test Wafer.	17
Figure 1.5	SAM Image of Cz-Si Wafer Showing a Dual-crack Along the Periphery.	19
Figure 1.6	Impact Testing Apparatus Including Impact Hammer, Wafer, and Microphone.	20
Figure 2.1	3-D Image of the Piezoelectric Transducer, with Cross-hatching for Vacuum Contact, Positioned Beneath a Sample Wafer.	25
Figure 2.2	Lock-In Functional Block Diagram.	26
Figure 2.3	Effect of Angular Misalignment Before CMP Pad Tip.	28
Figure 2.4	Initial Four Point Alignment Apparatus.	29
Figure 2.5	Initial Design of Fork Loading Stage for Quick Alignment and Wafer Replacement.	30
Figure 2.6	Modified Fork for Edge Scan Measurements.	30
Figure 2.7	Acoustic Probe Model with CMP at Tip of Quartz Pipe for Coupling.	31

Figure 2.8	Graph Showing Attenuation and Frequency Shifting Under Increasing the 5-Point External Bending Stress Applied to the Wafer [38]. This Experiment Illustrates a Sensitivity of the RUV Method to the Internal and External Stresses.	32
Figure 2.9	Probe Contact Force Leveling Out After Initial Increase in X-position.	33
Figure 2.10	A Physical Schematic of the Experimental RUV System.	34
Figure 2.11	An Electrical Schematic of the RUV System.	35
Figure 2.12	RUV Program User Interface Screen Shot.	36
Figure 2.13	Mutual Layout of the Transducer, Wafer and Probe in the RUV Setup.	37
Figure 2.14	RUV Parameter Shift Due to Increasing Vacuum Pressure Through Transducer, as Monitored by the In-line Vacuum Gauge Indicating Negative Pressure Created Between Transducer and Silicon Wafer. Insert Shows Broadening Bandwidth with Increasing Stress from Greater Vacuum Pressure.	38
Figure 3.1	Full Frequency Scan in 156mm x 156mm Cast Si Wafer.	42
Figure 3.2	Variation of the Resonance Peak Position Versus Edge Length of the Square Shaped Wafer. Dotted Lines – FEA Calculations, Dots – Experimental Data on Si Wafers.	43
Figure 3.3	(a-d) FEA Calculated Mode Shapes Corresponding to Peaks 1-4 Respectively as Seen in Figure 3.1.	44
Figure 3.4	Amplitude Variation of the RUV Mode Along the Wafer Edge Representing Peak 1 at 30 kHz (left) and Peak 2 at 45 KHz (right). (a) FEA modeling, (b) Experimental data.	45
Figure 3.5	(a) 30 kHz, (b) 45 kHz, (c) 67 kHz, and (d) 87 kHz Physical Mode Shape Reconstruction Comparison to FEA Results.	46
Figure 3.6	Possible Crack Propagation Directions (a) and (b) Single (c) Dual (d) Branched and Correct Elongation Procedure (e) Wafer with Initial Induced Crack (f) Same Wafer after Successful Elongation.	49

Figure 3.7 (a) Peak #2 Mode Showing a Small RUV Parameter Shift when a 6 mm Crack was Introduced to the Wafer's Edge (b) Peak #3 Mode Showing Larger RUV Parameter Variation on Same Cracked Wafer. 50

Figure 3.8 (a) Peak Shift Versus Crack Length Dependences for Three Vibration Modes on 125mm Wafer for the Center Edge Crack Location; (b) Variation of the Peak Shift with Stiffness of the Spring Element. (1) Mode #1 (40 kHz), (2) Mode #2 (58 kHz), and (3) Mode #3 (86 kHz). Notice that Mode Frequencies are Scaled up due to Reduced Wafer Size. 51

Figure 3.9 (a) FEA Calculated Variation of the Peak Position Versus Crack Length to a Center Crack Position for Vibration Modes #1, #2, and #3 (b) Same for a Crack at the Corner Position. 52

Figure 3.10 RUV Peak Shift from a 5mm Corner Crack Measured for (a) #2 and (b) #3 Frequency Modes. Notice that #2 Mode shows 55Hz Downward Shift of the Resonance Frequency compared to 19Hz Shift of the #3 Mode. 53

Figure 3.11 4 mm Corner Crack in Wafer 34A Contributing to the Shift of the # 3 Peak. 53

Figure 3.12 Crack Detection Run on a Set of 125mm x 125mm Cast Wafers with the Wafer #11 Possessing 10 mm Periphery Crack Identified by RUV Parameter Variations (1) Peak Position, (2) Peak Bandwidth, and (3) Peak Amplitude. 54

Figure 3.13 Sample of 200um Thick Cz-Si Wafers as Delivered from Vendor. Wafer 39 Clearly Shows Shifted Bandwidth and Frequency, Indicating a Crack. 55

Figure 3.14 Crack in Wafer 39 as Detected by the RUV System and Imaged Here Using the Sonix SAM. 56

Figure 3.15 Crack Elongation Apparatus Showing 125 mm x 125 mm Cz-Si Wafer in Clamping Apparatus with Pushing Rod, Attached to Z-stage, at the Wafer Corner. 57

Figure 3.16 Successful Elongation of Wafer Using Crack Elongation Machine. 58

Figure 3.17 Photo of Water Evaporation Around 20 mm Crack. 58

Resonance Ultrasonic Vibrations (RUV) for Crack Detection in Silicon Wafers for Solar Cells

William Dallas

ABSTRACT

The photovoltaic industry provides a pathway to allow renewable energy to meet world wide consumer energy needs. Past and present research and development on silicon based solar cells have helped make them the dominant player in the photovoltaic industry accounting for over 75% in 2005 as accounted by the US Department of Energy. One of the current technological problems is to identify and eliminate sources of mechanical defects such as thermo-elastic stress and cracks leading to the loss of wafer integrity and ultimately breakage of as-grown and processed Si wafers and cells.

The RUV method, developed at the University of South Florida, enables fast and accurate crack detection with simple criteria for wafer rejection from solar cell production lines. The RUV system relies on variation of modal vibration characteristics due to physical variations in the wafers caused by cracks. Ultrasonic vibrations are introduced into the wafer using a vacuum coupled transducer and received by an acoustic probe mounted along the periphery of the wafer. Cracks are detected by monitoring shifts in the resonance peak's frequency, bandwidth, and amplitude. In Cz-Si wafers it has been shown that increased crack length leads to a decrease in peak frequency and an increase in peak bandwidth and decreasing peak amplitude. Minimum crack length

sensitivity is related to the uniformity of the RUV parameters from wafer to wafer within a batch as well as system characteristics. Typically the RUV system is capable of detecting sub-millimeter length cracks. The use of auto loading and unloading allows the RUV system to achieve mass production level speeds of approximately two seconds per wafer. The RUV system has been successful in detecting cracks in single crystalline and multi-crystalline silicon wafers. Further development of the RUV system would solidify its place in manufacturing plants for non-destructive crack detection in PV cells.

The contributing work of the author toward the further development of the RUV crack detection method will be examined in this thesis.

Chapter One: Introduction and Background

1.1 Defining the Need for Renewable Energies

The worldwide dependence on fossil energy must be stopped. Fossil energy supplies are depleting and the world's consumption is growing at an alarming rate. Renewable energy must be brought to the forefront and given the opportunity to alleviate the need for non-renewable fossil based fuels. The increasing usage of electrical power and automobiles of developed and especially developing nations lacking strong environmental policies only increases the need for clean and renewable energy solutions. Numerous worldwide organizations are devoted to the goal of increasing the availability of renewable energy solutions by decreasing the cost through advanced research and development. Environmentally friendly energy sources have been in existence for centuries whether from a water mill helping with mechanical processing of food or goods or a wind mill pumping water for irrigation. Through modernization of the world's developed nations we have gone from a society that utilized our local available energy sources to one with a dependence on massive quantities of non-renewable foreign fossil fuels causing political, economical, and environmental turmoil. Local energy sources such as wind, water, or the sun must be taken advantage of if we plan on enjoying the same weather, air quality, and life expectancy in a hundred years that we do today. The

direct conversion of sunlight into electricity through the use of photovoltaic cells is helping reduce our dependence on fossil energy today. During times of increasing energy costs renewable energy sources are looked to as a means to save energy consumers from a crisis.

1.2 Silicon for Photovoltaic Cells

Solar cells and panels are currently available to provide direct conversion of solar energy into usable electricity. Solar panels are often connected to power grids for mass distribution or used in isolated applications. To compete with traditional fossil energy sources, the solar or photovoltaic (PV) industry is driven by economic reasons to make solar panels of the highest power conversion efficiency along with high reliability at the lowest possible production cost. Being the second most abundant material in the earth's crust and one of the most studied elements, Silicon (Si) has taken a dominant role contributing to over 75% of the entire production of solar cells. As an example of the marketplace today, single crystal Si technology offers solar cells with costs of $3 to $4 per peak Watt of power, at conversion efficiencies in the range of 18 to 20%. For lower quality multicrystalline silicon (mc-Si) solar cells with approximately 16% efficiency the price ranges from $2.50 to $3.00 per peak Watt. It is important to recognize that the silicon wafer is a large contributor, up to 75%, to the overall cost of the solar cell. In addition, the silicon raw material price has roughly doubled in the last two years due to a worldwide shortage of polycrystalline silicon feedstock. To compensate for the feedstock shortage, solar Si wafers are sliced thinner with thickness in the range of 80-200 microns.

These thinner wafers do not have the mechanical stability of the previous wafers and are more likely to break during handling. Wafer areas (a) have also been increased to reduce overall production costs and larger sizes up to 210 mm x 210 mm square shaped wafers are now available. These technological trends make wafer handling in production more challenging and reduce the yield of solar cell lines due to increased wafer and cell breakage. In-line wafer breakage also reduces equipment throughput as a result of down time and the need to stop and clean out machinery to remove broken wafers from the fixtures, which is typically a manual process. Wafer breakage during a production procedure can often lock up a whole process for minutes or longer for cleaning up the automatic belt conveyor and possibly cause costly damage of the equipment.

Research groups around the world are experimenting with numerous materials for use in photovoltaic cells. Thin-film materials deposited on a stable substrate, bulk silicon, and nanocrystalline silicon materials all have been used for solar cell fabrication. As previously mentioned with the rising cost in silicon, thin-film technologies that use uniformly deposited layers of semiconductor material have proven a worthy opponent to the popular bulk silicon technologies. Thin film materials used in making photovoltaic cells include cadmium telluride (CdTe), copper indium gallium selenide (CIGS), copper indium selenide (CIS), gallium arsenide (GaAs), as well as many light absorbing organic materials. The benefits of these non-silicon based technologies are evident but at present time crystalline silicon solar cells dominate the market due to low cost and high efficiency.

1.2.1 Mono-Crystalline Silicon

The ability to grow large silicon crystals with uniform crystal orientations has allowed continual advances in semiconductor devices. Single crystalline based solar cells are generally made using one of two methods: Czochralski growth or the Float-Zone method.

The Czochralski (Cz) method starts with a singe-crystalline Si seed from which growth of the bigger crystal will start. The seed crystal is lowered into a vat of high purity molten silicon contained within a quartz crucible. The seed is slowly raised from the vat at a controlled temperature while turning to maintain a cylindrical ingot. [1] Slower pull speeds often lead to larger diameter ingots reaching over 300mm in diameter and several meters in length which can then be sliced into wafers. One known issue in the Cz method is the contamination of oxygen in the silicon ingot from the walls of the quartz crucible. [2] In devices where oxygen contamination can significantly lower minority carrier lifetimes, such as conventional boron doped Si by creating boron-oxygen pairs trapping carrier electrons [3], other crystal growth methods needed to be realized. The Float-Zone (FZ) method of crystallization was first used in 1953 by Keck and Golay [4]. By zone melting an ingot of poly-silicon in contact with a single crystalline seed, a high-purity, low oxygen containing single crystal could be formed. With no crucible to contaminate the molten Si with oxygen, the FZ silicon ingots were found ideal for use in applications where high lifetimes were critical. Although the FZ silicon wafers had a lower oxygen concentration and higher lifetimes the mechanical stability of the wafers seemed lower. The higher susceptibility of FZ silicon wafers to thermal stress causing

slip dislocations and wafer warping has deterred IC manufacturers from relying on FZ silicon [5]. Due to its higher processing cost PV manufacturers also have traditionally stayed with Cz silicon.

1.2.2 Polycrystalline Silicon

Whereas single crystal silicon is ideal in terms of electrical qualities, its high cost of production in the cost sensitive PV market makes polycrystalline silicon (poly-Si) a pragmatic choice. The refining process of PV or IC grade silicon from metallurgical grade silicon (MG-Si) consists of chemical reactions with the 99% pure silicon in order to obtain the much higher purity levels needed for electronic devices. The resulting poly-Si may have small non-uniform grains of single crystal Si throughout. The effects of grain-boundaries on the electrical properties of PV cells has lead to the development of casting processes resulting in larger and more uniform grains. Increasing the grain size allows the minority carrier diffusion length to be effectively lengthened due to less interaction at grain boundaries. This has lead to the acceptance of poly-Si as an inexpensive alternative to single crystalline silicon for photovoltaic applications. The common methods for producing polycrystalline wafers are: the casting method, the Edge defined Film Growth (EFG) method, and the ribbon growth method.

The casting method simply introduces the molten highly pure Si to a mold where it is allowed to cool at a defined rate. The rate of cooling is said to influence the grain size along with other factors. The cast block is then cut with a saw into the wafers for PV cells. The block casting method has high (~30%) kerf loss due to the need to saw the

blocks into singular wafers as well as the introduction of surface damage. Due to these facts methods that limit the amount of wasted silicon were developed. It was assumed that methods that did not need the sawing step could save a large percent of the wasted silicon while eliminating the need for surface etching or polishing. Drawing silicon in the form of ribbons seemed to present an alternative to sawing.

The EFG method draws on similar techniques developed in the Cz-Si method. The cast silicon is pulled from a molten bath through a die to produce a hollow tube of poly-Si. The tube geometry is determined by the die shape and is usually a polygon with a relatively large diameter to allow laser cutting of individual wafers from each side. This process eliminates the need for sawing and saves silicon lost in the sawing process as well as reducing the surface roughness caused by the sawing which often leads to surface defects such as sub-surface micro-cracks.

The EFG method is similar to another ribbon-type technology usually called the string ribbon method. In this method two supporting 'strings' are used as supports for the vertically pulled ribbons of poly-Si material. Horizontal ribbon pulling methods such as the Silicon Film, developed by Astro Power, and Ribbon Growth on Substrate (RGS) developed by ECN are emerging technologies which may allow faster pull rates due to the use of a substrate material that can help control crystallization temperature [6].

1.2.3 Amorphous Silicon

The benefit of uniform crystal structure in electronic devices is evident so it may seem slightly abnormal to consider silicon's non-crystalline allotrope, amorphous silicon, as a prime candidate for electronic devices. Amorphous silicon (α-Si) does not form the uniform crystal structure present in the previously discussed allotropes. The random orientation of silicon atoms can be formed by plasma enhanced chemical vapor deposition (PECVD). The decomposition of gases, typically containing silane (SiH4), in a plasma yield thin film coatings of α-Si which may be deposited on a variety of surfaces at low temperatures [7]. A critical component of the α-Si deposition is the incorporation of hydrogen, which bonds with the loose dangling bonds in the amorphous silicon making hydrogenated amorphous silicon (α-Si:H) [8]. The use of α-Si:H in photovoltaic cells is limited by its relatively low conversion efficiency of ~10% when compared to crystalline Si cells with efficiencies of more than twice that. Another significant disadvantage of α-Si:H solar cells is a substantial photo-degradation after prolonged light soaking attributed to a meta-stable Staebler-Wronski effect [9]. Amorphous Si has found its niche market in low power, low cost, applications such as handheld calculators. Other applications of α-Si:H include taking advantage of its low temperature applicability on flexible substrates or as thin film transistors for displays which is currently substituted by poly-Si thin films in active-matrix LCD technology.

1.3 Fracture and Cleavage in Silicon

On a molecular level fracture occurs in materials when the applied force is equal to the cohesive stress binding individual atoms together. In this idealized model fracture occurs at a force several orders of magnitude higher than is noticed in practice. This was observed early in history to be due to the stress concentration effect of material flaws [10]. Fracture in highly ordered crystalline materials such as silicon along crystallographic directions can be viewed as cleavage. Cleavage in crystalline materials occurs along the crystal directions in which the lowest number of atomic bonds are present. Cleavage prefers the lattice planes with the lowest surface energy (γ_s), this results in the lowest amount of bonds needing to be broken [11]. In silicon the (111) and (110) crystal planes show the lowest resistance to fracture under a force of approximately 2.2 J/m^2 [12]. The fracture stress is related to the surface energy of the material by

$$\sigma_f = \left(\frac{2E\gamma_s}{\pi a} \right)^{1/2} \qquad \text{Equation 1.3.1}$$

where σ_f, is the fracture stress, E, is the Young's modulus, γ_s , is the surface energy, and a, is the crack area [10]. It has been shown that the surface energy for the (110) and (111) crystal planes is the lowest, 1.73 J/m2 and 1.44 J/m2 respectively, of all planes.

In crystals with defects, such as microcracks, the amount of force necessary to cause a fracture is decreased. The fracture mechanics of single crystal silicon can readily be applied to individual grains of polycrystalline material if crack lengths are less than average grain size. Numerous physical and numerical models exist for the prediction of fracture parameters such as crack propagation speed [12], direction [11], as well as the

atomistic mechanisms of fracture [13] in silicon. The use of these models has not been of sufficient help to the manufacturers of PV cells, who work with higher levels of impurities and defects in varying crystal structure silicon, to eliminate the need for crack detection methods in the manufacturing line.

1.4 Mechanical Characterization Methods

Various crystal growth methods such as Czochralski, Float Zone, casting, Edge-defined Film-fed Growth (EFG) and ribbon are in use with goals of minimizing cost while maximizing cell efficiency. The impeding challenge of demand outstripping supply for silicon feedstock has lead PV suppliers to move to thinner wafers to save expensive silicon. A large challenge going to thinner cells is the deterioration of the structural integrity present in thicker cells. Cracked wafers are becoming more common and methods to detect and remove damaged wafers are in great need. Whether the solar cells are based on single crystalline or polycrystalline type silicon, similar manufacturing steps lead to producing the finished cells. Many of these steps induce additional stresses on the already weakened wafers due to ingot and brick sawing and chemical etching after depositing thin dielectric or metal films, wafer annealing, soldering of contact strings and lamination of cells into solar panel modules. Wafer/cell damage in the form of periphery cracks can be initiated by any of these processes and serves as the starting point for fracture. Various research groups have presented laboratory results of experimental methods for crack detection in Si wafers.

1.4.1 Mechanical Bending Tests

Mechanical bending tests induce physical stress on wafers that is at or above a predefined critical stress value. It is well known that defects in materials act as stress concentration centers often serving as the source of fracture [10]. Micro-cracks, introduced through manufacturing processes, act as defects and can lead to fracture under critical stress levels. Numerous mechanisms for inducing stress in wafers by bending exist including: point bending, biaxial point bending [14], double ring bending [15, 16], 3-line bending [17], 4-line bending [15], twist test bending [18], and any other geometric arrangement of opposing forces. An example of these bending tests is illustrated in figure 1.1 along with stress distribution maps.

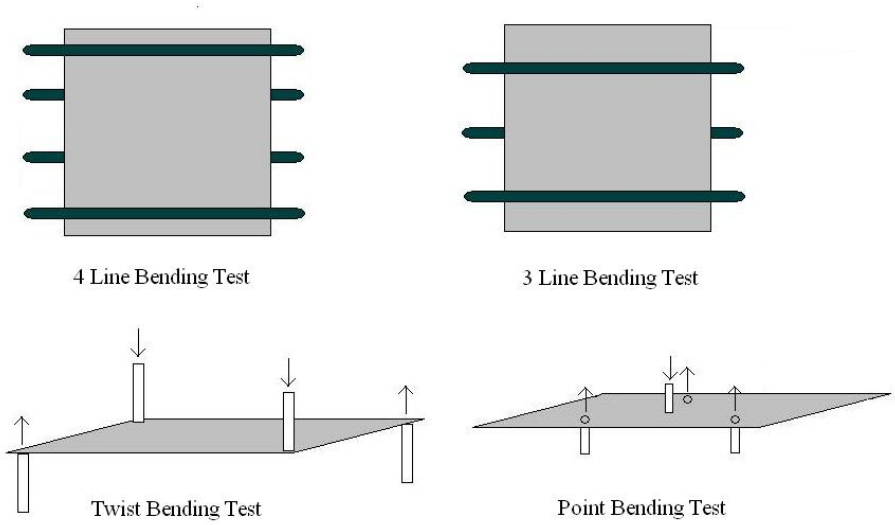

Figure 1.1 Four Different Mechanical Bending Tests.

Each of these bending tests introduces their own unique stress field in the wafer. In order to gain a uniform comparison of the fracture strengths of different sized wafers analyzed on different bending tests the authors in [19] used the relation: $\sigma_{f,1}$ $\sigma_{f,2}$

$$\frac{\sigma_{f,1}}{\sigma_{f,2}} = \left(\frac{V_2}{V_1}\right)^{\frac{1}{m}} \qquad \text{Equation 1.4.1}$$

where $\sigma_{f,1}$ and $\sigma_{f,2}$ are the fracture strengths of the two specimens and V_1 and V_2 are the respective volumes. These breakage type tests rely on the fact that micro cracks have been shown to reduce the critical external stress applied to a wafer to cause fracture. Wafers that do not break are considered good and allowed to continue for further processing. Loading the wafer can initiate its breakage in areas with high thermo-elastic stress, which is not acceptable. These bending or twist tests physically load the wafer to a critical breakage point for damaged wafers. These types of crack identification have evident disadvantages because a critical load is a complicated function of the wafer geometry and crystal type (single versus polycrystalline structure) and have low sensitivity to short mm-length cracks. Solar processing steps (sawing, etching, P-diffusion, antireflection layer coating, contact fringes, and back contact deposition) induce numerous manufacturing flaws that can contribute to a lowering or increasing of the critical load. As can be seen in Figure 1.1 none of the available mechanical bending tests can singularly apply a stress field that would have an equal chance of detecting cracks positioned along the periphery as well as in the center at all wafer orientations. Finally, the mechanisms for applying the physical stress to the wafers must be very accurate and able to maintain stress levels with varying wafer thickness or warping and

possibly slight changes in orientation due to the low-cost approach to wafer handling adopted by the PV industry to compete with other energy sources.

One proposed method of applying a non-uniform stress field to the wafer under test was developed by the authors in [20] at the National Renewable Energy Lab (NREL). This method involves illuminating the wafer surface in a non-uniform manner and in effect locally heating the wafer surface. This uneven heating over the wafer surface will result in tensile and compressive stresses relative to the heating zone. The thermally induced stress can be controlled via lamp intensity and local convection cooling of the wafer to achieve stress levels high enough to fracture wafers with sufficiently large cracks. The authors do not mention specific time lengths that the wafer would need to be under illumination to achieve sufficient stress levels but mention they can be attained at 'high-speeds'. The side effects of the local heating are not discussed but mention of possible beneficial uses include pre-gettering and impurity dissolving.

1.4.2 Optical Transmission

The optical μ-crack detection method in development at the University of Konstanz, Germany is said to be viable as an inspection tool for in-line characterization of wafers and finished cells [14]. In this method the subject silicon wafer is placed in front of a broad spectrum high intensity flash-light with an intensity of approximately 1000 suns. A high resolution CCD camera is used to detect the optical transmission through the wafer.

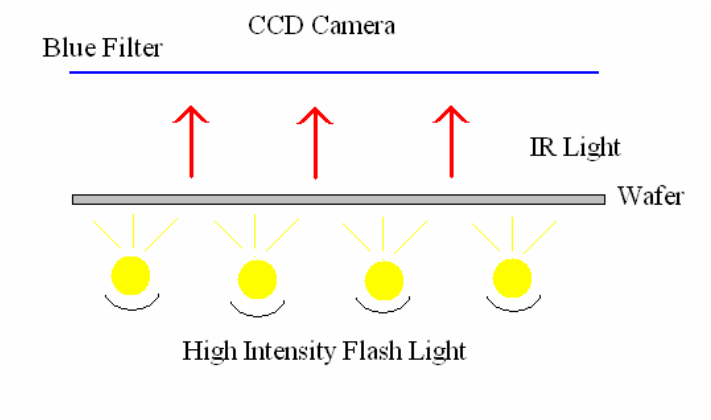

Figure 1.2 Optical Transmission μ-crack Detection Apparatus.

The infrared portion of the light passes through the wafer and is detected by the CCD camera with varying intensities related to wafer thickness and crystal structure. For crack widths less than 1 μm the infrared detection system is suitable, yet for more widely opened cracks the visible portion of light may be detectable by the CCD camera.

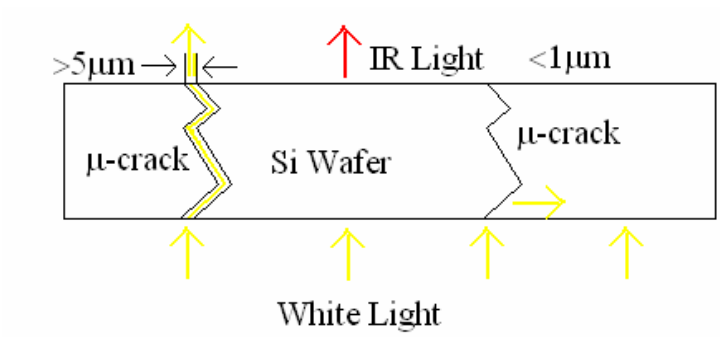

Figure 1.3 Diagram of μ-crack Widths and Detection Mechanisms [14].

In this case it was shown that the use of a blue filter was necessary to block out the infrared portion which overpowered the image and did not allow for 'open' crack detection. It is worthwhile to notice that here the definition of a μ-crack is viewed as any

length crack with an opening width measured from 1um (closed crack) to 5-10 μm (open crack). Crack lengths in the test experiments were shown to be on the order of tens of millimeters. The infrared waves passing through a polycrystalline silicon wafer showed interference at grain boundaries in an effect that was said to be favorable for calculation of crystallinity factors [21]. Due to this effect it is nearly impossible to distinguish 'closed' cracks in polycrystalline wafers. Crack detection in finished cells was highly impeded by the metallic aluminum backside contact.

1.4.3 Photoluminescence and Electro-luminescence Imaging

Luminescence in semiconductors is the result of electron-hole recombination giving off a photon. The reverse process of excitation of an electron from the valance band to the conduction band with the assistance of the energy of a photon is the basis of which photovoltaic cells work. Photoluminescence (PL) is the result of electron-hole recombination as a result of electron excitation from photon absorption [1]. Taking advantage of this property, the authors in [22],[23] used photoluminescence imaging to view process defects in silicon wafers. Using a 15 W/815 nm diode laser to excite the sample, wafer properties such as carrier lifetimes and defects (such as cracks) can be detected. Photoluminescence images were detected using a cooled CCD camera with a 1000 nm long-pass filter to remove from the image the reflected and scattered laser light. The image could be collected from either side of the sample but the authors chose a

single sided excitation/collection method. Imaging times of 1.5 seconds were achieved and time reduction was being worked on.

In a similar method also examined by [23], electroluminescence imaging has also been looked at as a method for fast detection of material flaws and cracks. Electroluminescence (EL) is a form of luminescence in which electrons are excited into the conduction band through the use of an electric current, commonly under the forward bias of the cell's p/n junction [1]. Again, the luminescence comes from the recombination of the electron-hole pair giving off a photon. In silicon solar cells under forward bias the emitted photons due to band-to-band recombination show a peak with wavelength at 1150 nm [24]. This emission band can be captured by a cooled CCD camera. Lower emission was seen around defects that lower the minority carrier diffusion length. Recombination at grain boundaries, effectively decreasing minority carrier lifetime [25], would likely cause the confusion of microcracks with grain boundaries in EL images.

Though luminescence methods are fast and non-destructive, other types of defects such as surface scratches and dislocations may interfere and mislead crack identification. Additionally, optical detection methods rely on graphic detection and automation which means that fast image recognition software needs to be employed.

1.4.4 Infrared Lock-in Ultrasound Thermography

In Ref. [26], the authors proposed inducing ultrasound vibrations of a fixed 20 kHz frequency into silicon wafers. The authors proposed that under this excitation, heating can be observed with an infrared camera around cracks. Several problems with this system have limited its acceptance into use. In order to detect open cracks the sample needed to be covered in a layer of absorbent black paint to block the IR signal from masking the crack. The small size of the micro-cracks was also said to likely provide little local heating and detection would be limited. Although this method of crack detection was shown to be viable under certain conditions, due to the constraining issues involved and the long time of measurements (minutes) for data acquisition, the method was abandoned for in-line crack detection usage.

1.4.5 Scanning Acoustic Microscopy

The use of acoustics to study materials dates back to the beginning of this century. High-frequency, over 20 kHz, acoustic waves are referred to as ultrasonic, meaning above the range of hearing. The use of ultrasonic waves has been highly developed for the use in military applications such as sonar. Ultrasonic waves have also been used in applications such as non-destructive analysis of materials and in the healthcare profession to view a fetus before birth. The use of ultrasonic waves in the small scale analysis of

materials started in the mid 1970's and a history of the development of the acoustic microscope can be readily found in [27].

The principals of the modern scanning acoustic microscope (SAM) will be briefly discussed as they can be found in detail in numerous sources elsewhere [28],[29]. The SAM operates by emitting high frequency acoustic waves directed at a sample. The broad-band ultrasonic waves are emitted by a piezoelectric transducer with a focusing aperture. The focal point of the acoustic beam is set to the desired depth of investigation by moving the transducer in the vertical z direction. Focus at an apparent depth can be achieved by viewing the output signal in relation to the initial time of the impulse. By moving the z stage and noting the so-called time of fight, one can focus the ultrasound signal at some specified distance in the material under test.

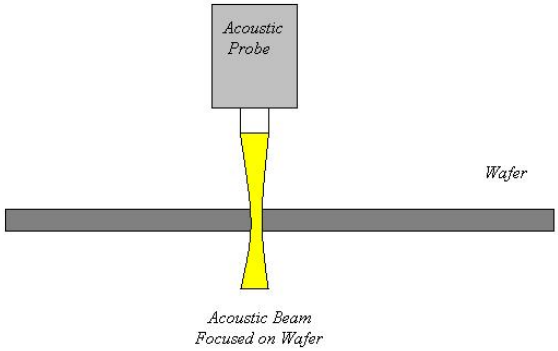

Figure 1.4 Relative Beam Shape of Acoustic Signal as Emitted from Transducer and Focused Near the Center of the Test Wafer.

This time can be calculated if the material-under-test as well as the coupling medium sound velocities are known. In many of the modern day systems the emitting transducer also serves as the receiving transducer upon reflection of the ultrasound pulses. The reflection mode operation allows the operator to focus the acoustic signal at a specific depth in the material under test and achieve a two dimensional map at this surface depth. The transmission type of operation, which uses a second transducer beneath the sample, does not allow for this type of depth study yet allows mapping of the entire thickness at once. Determining the depth of a feature is not possible with this detection method [30].

Material characterization is accomplished through the fact that when the ultrasound wave encounters an interface between materials with different acoustic impedances (Z) reflection and transmission both occur. Acoustic impedance is defined as

$Z = \rho * c$, [30] Equation. 1.4.5 a

Where, ρ, is the density of the medium and c is the velocity of sound through the medium, both well studied material characteristics. The difference in Z between the two materials determines how much of the signal will be reflected and how much will be transmitted. The percentage of the transmission (T) and reflectance (R) amplitudes can be calculated as:

$$T = \frac{2(Z_1)}{(Z_2 + Z_1)} \quad , \quad R = \frac{(Z_2 - Z_1)}{(Z_2 + Z_1)} \qquad [30] \qquad \text{Equation.1.4.5 b}$$

Where Z_1 and Z_2 are the respective acoustic impedances of the two materials the wave is transferring through. Large reflectance occurs when traveling from a material of

low acoustic impedance to one of high acoustic impedance or the opposite. Due to this fact, the SAM technique is highly sensitive with respect to any structural openings in solids such as voids, cracks, or delaminated surfaces, which have negligibly small acoustic impedance leading to a high intensity reflected beam according to Equations (1.4.5 a & b). The propagation of the ultrasound signal from the piezoelectric transducer to a sample in air poses a significant problem for SAM due to strong absorption of the high-frequency acoustic waves in air. For this reason, in the commercially available SAM made by Sonix, Inc., the sample and the transducer are immersed in deionized water which acts as a coupling medium. Although there is still relatively high reflection from the water to sample surface it is nowhere near the losses that would take place through air coupling.

The ability of the SAM to show non-uniformities within a sample has made it an ideal tool for characterizing electronic devices [31]. In the current application of crack detection, the SAM can map a PV wafer and shows a definite contrast difference over a crack in the material. Long measurement times restrict the SAM's usage to research and development type applications, where 20 minute scan times are acceptable. Reflectance caused by the crack is seen in the image map and has been an invaluable tool for confirming crack existence, size, and location as can be seen in Figure 1.4.

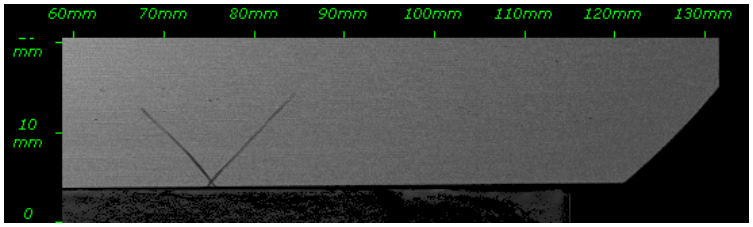

Figure 1.5 SAM Image of a Cz-Si Wafer Showing a Dual-crack Along the Periphery.

1.4.6 Impact Testing

In a method somewhat similar to the RUV technique, the audible frequency response after a physical impact on a Cz-Si wafer is analyzed. The silicon wafer is placed on a piece of convoluted foam with a microphone positioned 2 cm above the wafer. The wafer is struck with a piezoelectric impact hammer with a vinyl tip to measure impact force. The audible frequency is detected with a microphone and sent to signal analysis software [32]. A picture showing the impact testing apparatus is shown in figure 1.5.

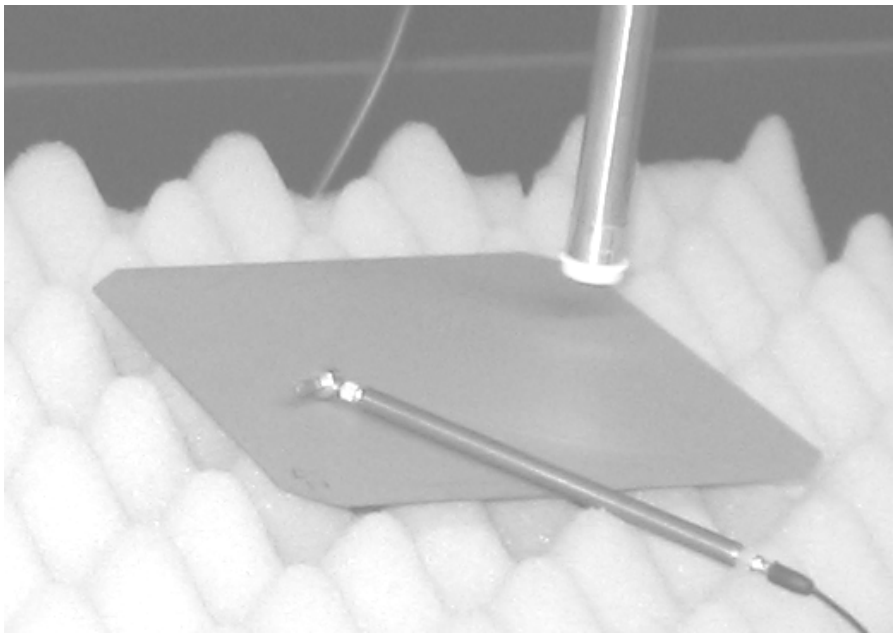

Figure 1.6 Impact Testing Apparatus Including Impact Hammer, Wafer, and Microphone.

The audible frequency response of a cracked wafer is shifted downward and the amplitude is decreased as well as the bandwidth of the peak broadening. This is the same

response noted for the RUV system which works at ultrasonic frequencies working on similar physical characteristics. This technique has been shown to detect large cracks over 10 mm in length and requires further development. Impact testing is being pursued by Dr. Daniel Hess's research group in the department of mechanical engineering at USF.

1.5 Finite Element Analysis

The finite element analysis (FEA) approach to solving engineering dynamic problems has been instrumental in evaluating the specific vibration modes of square shaped silicon wafers for PV applications. FEA makes use of computers for heavy calculations of complex mechanical problems, modeled by partial differential equations, by breaking them down into a finite number of smaller, yet still finite, pieces. Although the vibration of a body may be better modeled by taking into consideration the effects of each and every element that has any contribution to its reaction to stimulus, an approximation using fewer elements often leads to a much more solvable problem without significantly sacrificing accuracy. By clearly defining a set of specific material properties within the FEA based program ANSYS, it is possible to model the vibration of a body under forced vibration. Definition of the precise geometry of the body under analysis is the first step in using FEA. Following a geometric definition of the body, the material properties used in the analysis of the body are defined which include elastic modulus, Poison's ratio, and the material density. Definition of the type of mesh as well as the size of the mesh elements is defined according to the size, shape, and complexity of the body. By solving

the numerous differential equations responsible for the motion of each element simultaneously, solutions to cyclical stimuli can be modeled.

The number of papers presented on crack detection techniques in silicon has increased significantly over the last year following the increased interest of PV manufacturers in cost control mechanisms. The relative undeveloped nature of the field of fast crack detection in silicon wafers leaves numerous openings for new technologies, like the RUV system, to become standard and widely accepted. Currently there are no stand-alone candidates for fast in-line crack detection. Several methods hold promise upon further completion of stated issues. Developments in current technologies may lead to a leader but at present several of the mentioned technologies offer distinct advantages and disadvantages as outlined in Table 1.1. The RUV technique stands out due to its high sensitivity of detection and unique mechanism for measurement incorporated with fast analysis times. Through the continued research and development on the RUV system, fast and concise crack detection may become a reality.

Table 1.1 Comparison of Mechanical Characterization Methods.

Detection Technique	Approach	Time of measurement	Minimum crack length	Limitations	References
RUV	Acoustic resonance modification	2 seconds	sub-millimeter	Requires smooth coupling surface	[33]
Mechanical Bending Twist Test	Wafer stressing	seconds	millimeter size	Non-uniform stress may miss cracks	[14], [15, 16], [17], [18]
SAM	Ultrasound imaging	tens of minutes	sub-millimeter	Good for R&D use	[31]

Table 1.1 (continued)

Optical Transmission	IR light transmission	seconds	millimeter	Al coating inhibits detection, ineffective for poly-Si	[14]
Optical stressing	Optically induced stress	seconds	sub-millimeter	High temperature stress	[20]
Photoluminescence	Lowered PL intensity at crack	1.5 s	sub-millimeter	May misinterpret other defects as cracks that are caused by lowered minority carrier lifetimes.	[22],[23]
Electroluminescence	Lowered EL intensity at crack	seconds	sub-millimeter		[23]
Infrared Lock-In Thermography	Local heating from ultrasound	minutes	millimeter	Time intensive, sample prep.	[26]
Impact testing	acoustic response to mechanical impact	tens of seconds	>10mm	Undeveloped	

Chapter Two: Resonance Ultrasonic Vibration System

2.1 Development of the RUV System

The current method of crack detection using ultrasonic vibrations induced into a wafer was developed based on a previous system for stress diagnostics in full size IC and PV grade silicon wafers [34]. The previous system excited the wafer from beneath using a piezoelectric transducer that was vacuum-coupled to the wafer. The ultrasonic vibrations were mapped across the wafer's surface using a non-contact acoustic probe and indications about wafer stresses could be drawn. The technique was adapted for silicon solar cell wafers when a need was seen for the development of an inline stress detection tool with experimental justification on EFG wafers [33]. Rearrangement of the system for the measurement of longitudinal vibrations was accomplished by reorienting the acoustic probe and is detailed in [34].

The RUV system, as arranged for longitudinal vibration detection, consists of a piezoelectric transducer which is vacuum-coupled to the sample wafer. The transducer has crosshatching which spreads the pulling force of the vacuum around a larger area of the wafer as seen in figure 2.1.

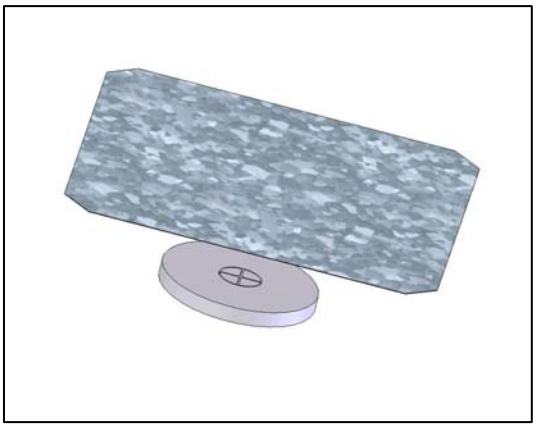

Figure 2.1 3-D Image of the Piezoelectric Transducer, with Cross-hatching for Vacuum Contact, Positioned Beneath a Sample Wafer.

The transducer is fed a signal from a computer controlled function generator (WaveTec 10 MHz DDS 29). The function generator signal is amplified by an audio amplifier (Samson Servo 260). The transducer induces the longitudinal vibrations into the wafer and standing waves are set up in the wafer at physically governed resonance frequencies. The transducer frequencies used range from 10 kHz to 100 kHz. Longitudinal vibrations were detected by a broad-band acoustic probe. The acoustic probe consisted of a small transducer (pinducer) coupled to a tuned quartz pipe used for electrical signal isolation. The acoustic probe was placed in direct contact with the center edge of the test wafer and the resultant signal from the probe was fed into a lock-in amplifier (Stanford Research Systems SR-850).

The lock-in amplifier allowed the relatively small micro-volt scale output AC signal from the pinducer to be recorded and extracted from a high noise environment. The lock-in amplifier needs two signals to make accurate measurements. The signal coming from the function generator driving the transducer must also go to the lock-in reference input for comparison of the frequency and phase of the signal from the acoustic

probe. Once the signals are sufficiently amplified and conditioned, the phase sensitive detectors (PSD) multiply the lock-in reference signal by the probe output signal. The use of two PSDs is critical to obtaining a phase independent output signal. The output of the two PSDs is two distinct sine waves, one at the sum frequency and one at the difference frequency. Low-pass filters then remove the high-frequency component of both signals. If the difference in frequency between the reference signal and the detected signal is zero, a DC component will exist in the difference signal. The lock-in makes use of narrow-band filters and phase-sensitive detection to detect the low voltage signal amongst the high background noise [35].

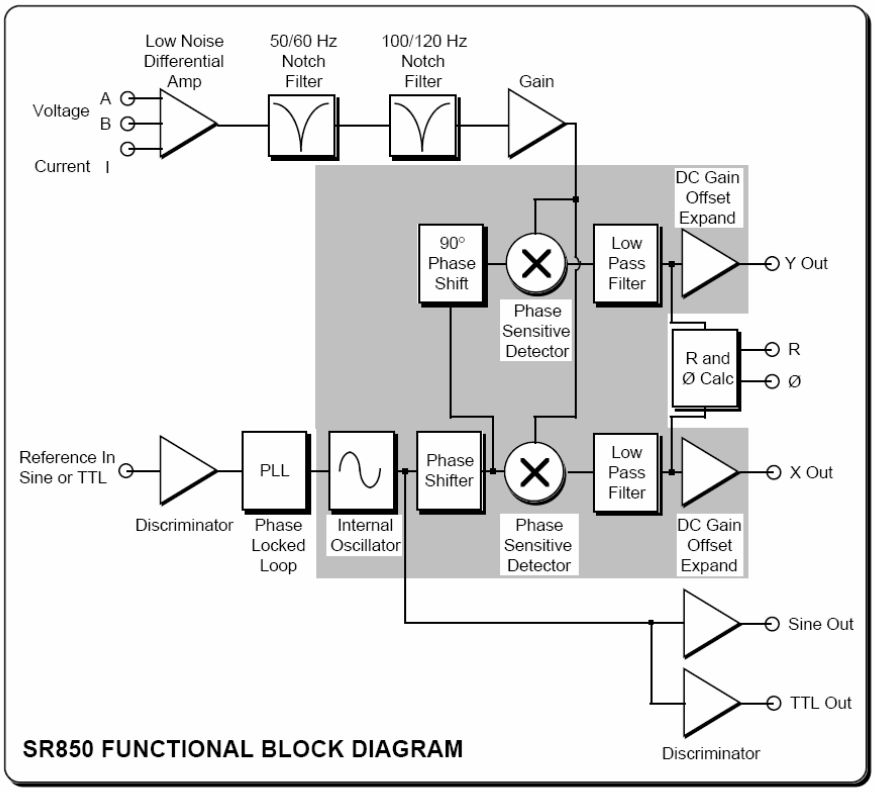

Figure 2.2 Lock-In Functional Block Diagram.

A custom made Windows-based computer program, designed by Dr. Igor Tarasov, allowed user selection of frequency sweep parameters and view results on-screen. The initial RUV system was shown to work for detecting different stress levels [36] as well as cracks [33]. Uniformity among results needed to be improved and the next section explains some of these additions to the RUV system.

2.2 RUV System Upgrades

The continued development of the RUV system was necessary as new experiments were devised and new wafer geometries were tested. The initial development of the experimental RUV system showed considerable potential for crack detection and further development was necessary to design an industry ready crack detection system.

2.2.1 Introduction of Adjustable Wafer Alignment

Wafer alignment in the original RUV system was accomplished by either visually aligning the wafer with the transducer table or using reference points and measuring distances between points. Needless to say alignment issues were a problem that needed to be addressed. The affects of misalignment of the acoustic probe with respect to the wafer's edge were studied. The acoustic probe was turned at $1/10^{th}$ degree intervals in one direction. Due to the symmetric nature of the system the opposite measurement was omitted and assumed to be similar. The total rotation of half a degree showed a decrease

in the RUV amplitude by a factor of 4 as illustrated in Figure 2.3. The following system upgrade solved the problem of wafer-probe misalignment and greatly reduced this undesirable effect.

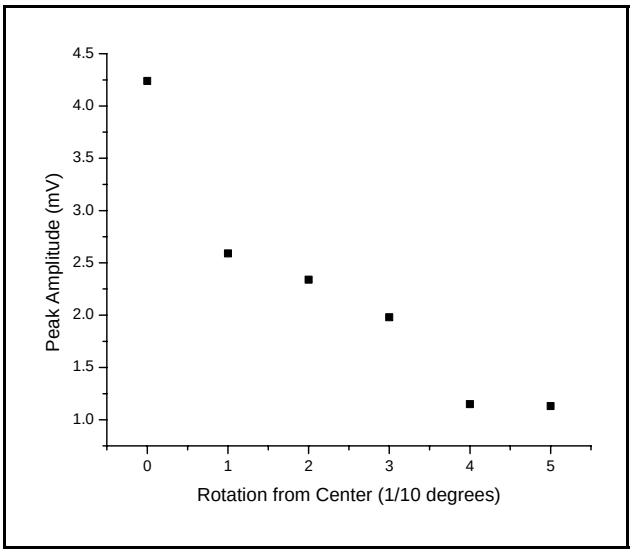

Figure 2.3 Effect of Angular Misalignment Before CMP Pad Tip.

The first improvement to be made was the removal of manual wafer alignment. Although the RUV technique is only slightly vulnerable to low angle misalignments, the issue still needed to be addressed. First a four-corner adjustable alignment apparatus was designed and fabricated. This is presented in Figure 2.4. Four adjustable brackets were fabricated that could be adjusted for wafer size to allow alignment. Measurement marks were made on the brackets that represented different standard sized wafers. It was adjustable for various wafer sizes yet required time consuming set-up measurements when going from one wafer size to another.

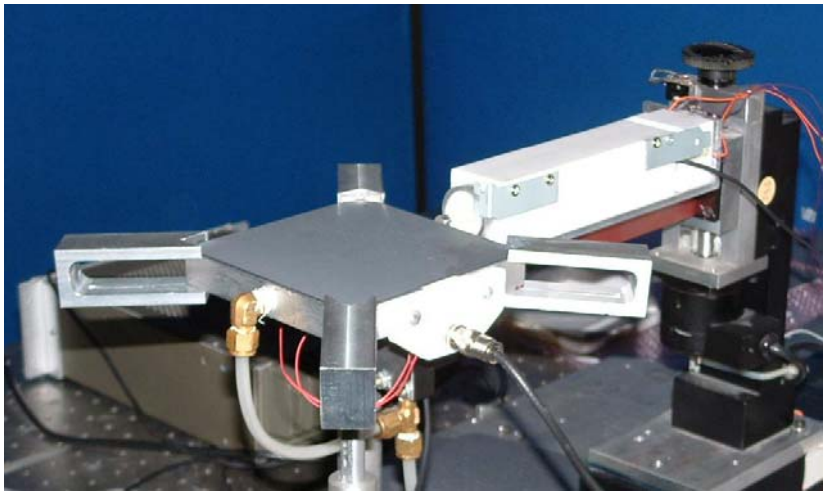

Figure 2.4 Initial Four Point Alignment Apparatus.

2.2.2 Automatic Loading/Unloading

The tedious nature of this design influenced the design of a faster alignment apparatus that could possibly be used with an automatic loading mechanism. A multi-leveled fork was designed that could accommodate several standard sized PV wafers (Figure 2.5). The fork acted as a wafer stage and the transducer could be raised and lowered in the vertical direction to load and unload the wafers in a controlled manner using a high precision Z-stage with a stepper motor operated by a programmable controller. The Z-stage was used to vertically lift the wafer from the holder using the transducer, locating the wafer in the Z-direction with 1 micron accuracy and after measurement returning it to the holder. Later an electrically controlled vacuum valve was incorporated to allow the full program control over the entire measurement process.

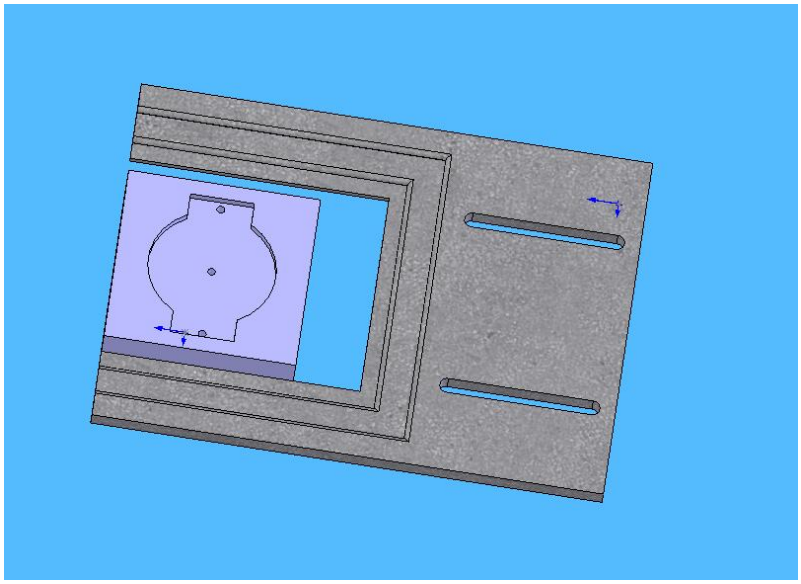

Figure 2.5 Initial Design of Fork Loading Stage for Quick Alignment and Wafer Replacement.

Further requirements for edge scan measurements lead to the modification of the fork by removing one side to allow for probe access. Edge scans with the probe moving along the edge of the entire wafer would now be possible.

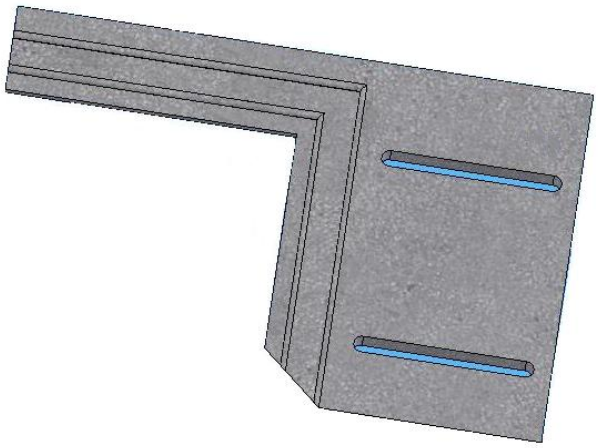

Figure 2.6 Modified Fork for Edge Scan Measurements.

2.2.3 CMP Tip and Elastic Element

In an additional measure of safety an elastic couple between the quartz pipe tip and the wafer was used in order to further minimize rotation misalignment affects as well as compensate for minute wafer edge non-uniformities. Several materials were looked at as a coupling medium but the optimal solution for high transmission and minimal rotation misalignment affects turned out to be a coupon of single layer chemical mechanical planarization (CMP) pad, used in IC industry in CMP processing technology. The coupons had a sufficient acoustic transmission, alleviated the rotation problem, and already had an adhesive on one side (Figure 2.7). Further RUV work was all done using a CMP tip on the acoustic probe.

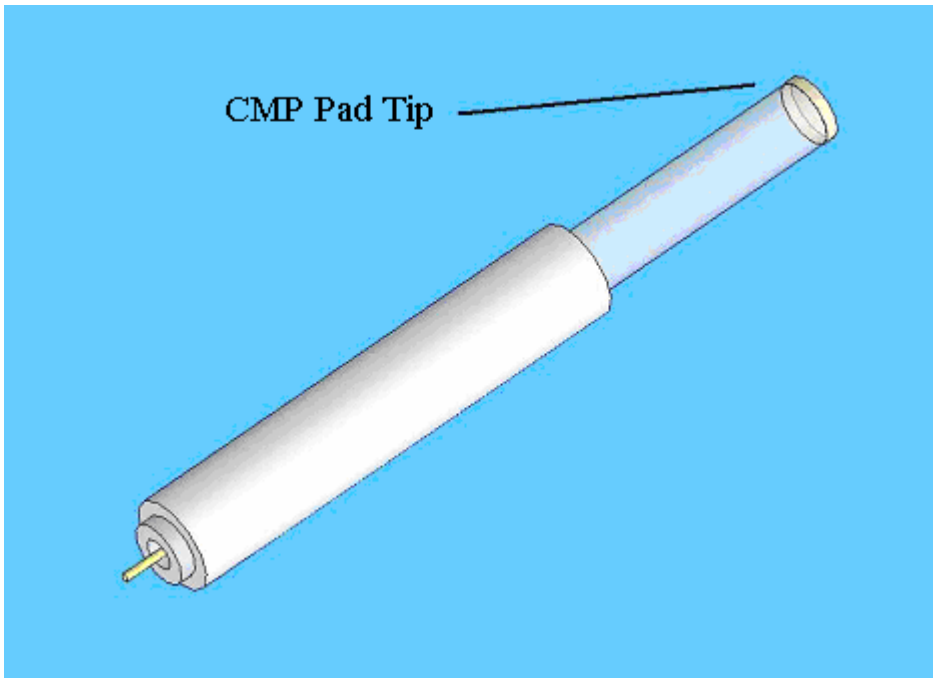

Figure 2.7 Acoustic Probe Model with CMP at Tip of Quartz Pipe for Coupling.

It was noticed early on in the experiments that the RUV parameters (amplitude, peak position, and bandwidth) could be altered by applying external stress to the wafer [38]. This was performed using a 5-point bending test and confirmed by statistical experiments of the RUV parameters compared to in-plane stress in EFG wafers [38]. The variation of the RUV peak can be seen in figure 2.8. It is clear that different negative pressures between the wafer and transducer could also noticeably disturb the RUV testing results as seen later in figure 2.14.

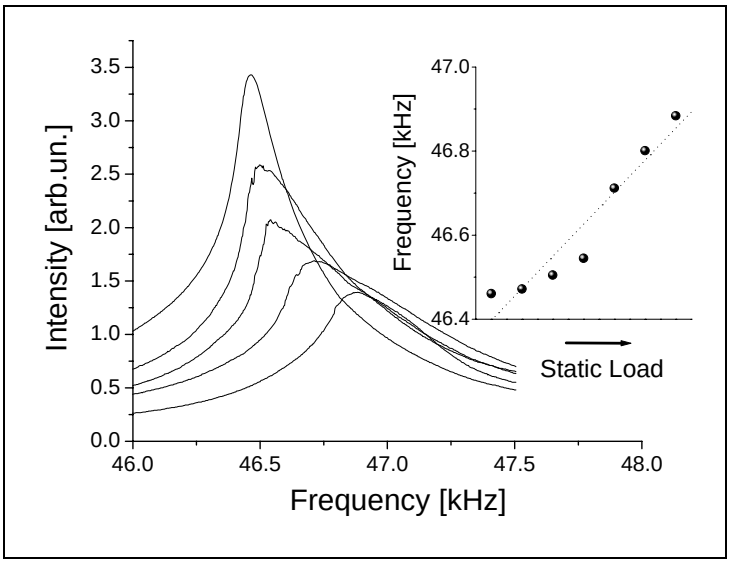

Figure 2.8 Graph Showing Attenuation and Frequency Shifting Under Increasing the 5-Point External Bending Stress Applied to the Wafer [38]. This Experiment Illustrates a Sensitivity of the RUV Method to the Internal and External Stresses.

In order to minimize these two effects and attain a uniform loading force between the probe and wafer a spring element and force sensor were introduced. The force sensor allowed us to calibrate the contact force between the wafer and probe. We found that above a certain x-position, spring element relaxation, the signal amplitude leveled off and

remained constant. Above a certain force, related to displacement by $F = -kx$, we saw stabilization of the CMP tip and amplitude remained constant. From this information we were able to limit the use of the force sensor to strictly calibration tasks and rely on x-position for uniform probe force.

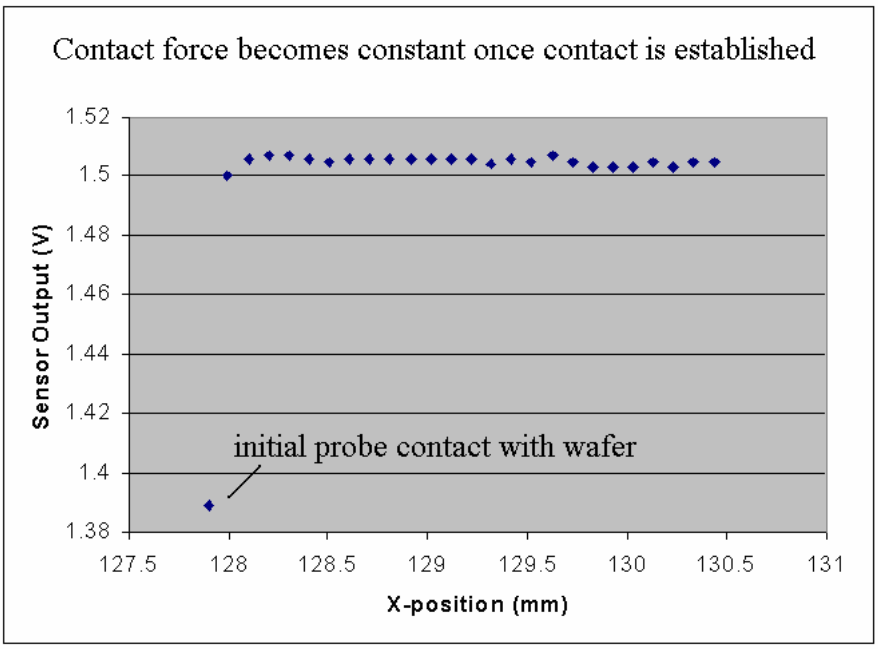

Figure 2.9 Probe Contact Force Leveling Out After Initial Increase in X-position.

2.2.4 Periphery Scans

As mentioned in section 2.2.2 there was a need for the ability to take measurements along the entire length of the edge of a wafer. Initially edge scan measurements had to be taken using the manual alignment procedure. The use of the manual alignment procedure for taking edge scans was especially tedious due to the extreme accuracy of alignment needed when taking signal amplitude measurements over

the entire edge of a wafer. Incorporation of a programmable y-stage, moving parallel to the wafer's edge, allowed the entire wafer/transducer/holder apparatus to be moved perpendicular to the acoustic probe. The additional movement required adaptation of the wafer holder fork as seen in figure 2.6. Critical alignment of the wafer was now as easy as placing the wafer in the wafer holding fork. Resonance peak amplitude was measured with incremental steps of the y-stage, as small as 1 mm along the periphery of the wafer. Edge measurements could now be precisely controlled from the computer via the y-stage stepper motor.

2.3 Current System Description

Resonant Ultrasonic Vibrations are induced into an as-cut or processed silicon wafer of symmetrical geometry through a vacuum coupled high frequency piezoelectric transducer beneath the wafer as illustrated in Figure 2.5.

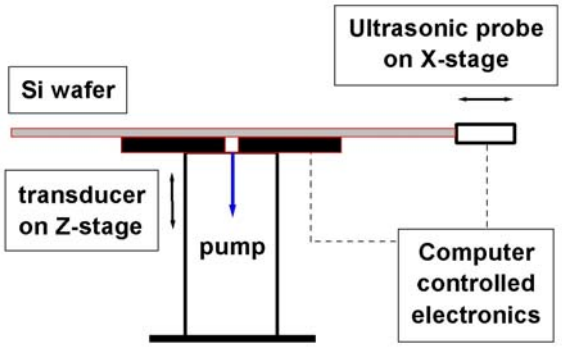

Figure 2.10 A Physical Schematic of the Experimental RUV System.

The transducer frequency can be swept in the ultrasonic range from 20 kHz to 100 kHz. Transducer frequency sweep parameters are user definable through the windows based operating program. The computer sends the frequency sweep parameter command to the WaveTec function generator. The function generator main output is fed into the Samson Servo 240 audio amplifier prior to being sent to the piezoelectric transducer. The function generator also provides a reference signal to the Stanford SR-850 lock-in amplifier for comparison to the output signal of the acoustic probe in the lock-in algorithm.

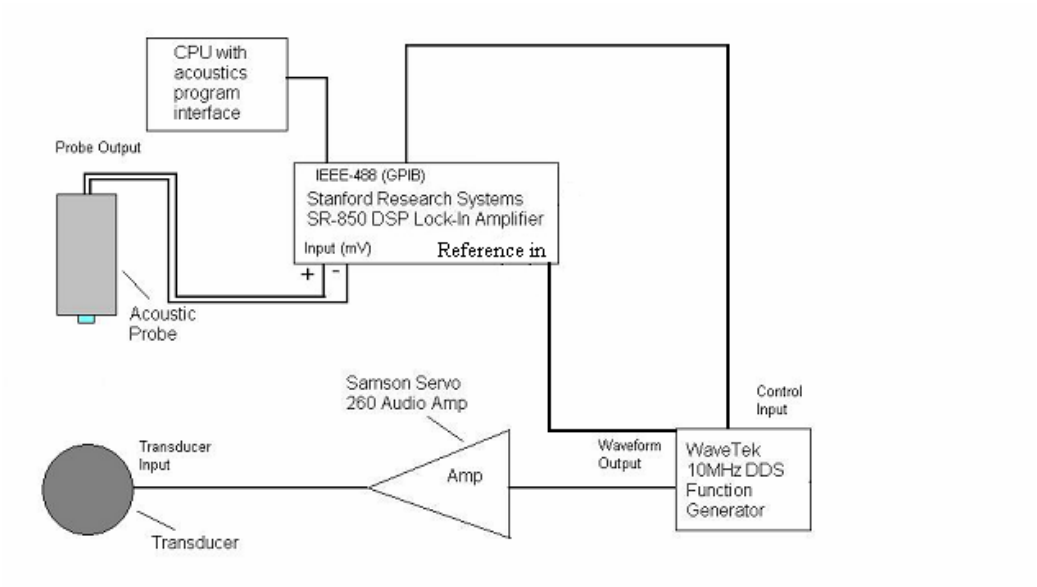

Figure 2.11 An Electrical Schematic of the RUV System.

Standing longitudinal waves are set up at resonance frequencies with peak positions controlled primarily by the wafer's geometry, size, and material's elastic characteristics. The differing physical attributes of each Si wafer lead to altered resonance mode shapes including peak position, peak bandwidth and peak amplitude.

The RUV vibrations are detected using a broadband ultrasonic probe. The probe consists of a small transducer (pinducer) attached to a quartz pipe for electrical isolation. At the tip of the quartz tip, which contacts the wafer's edge, is a small coupon of CMP material that is the same diameter as the quartz pipe. The purpose of which was explained earlier. The probe is attached with a controlled force to the edge of the wafer. Stepper motors allow synchronized movement and precise positioning of the wafer and probe for RUV measurements. The entire system is computer controlled and programming devices are operated by Windows-based original software. Figure 2.12 shows the RUV user interface including controls for stage movement (X,Y,Z), frequency scan parameters, vacuum switch controls, kinetics measurement controls, and automatic mode options for repeat measurements.

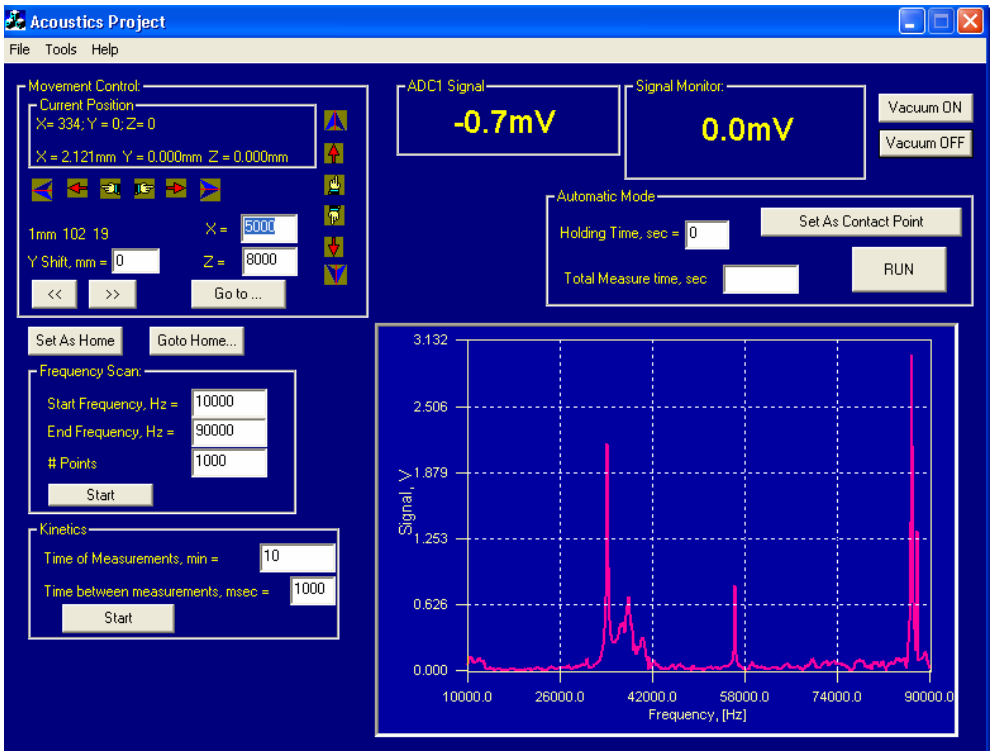

Figure 2.12 RUV Program User Interface Screen Shot.

The transducer beneath the wafer serves as both a holding stage via the vacuum coupling with the wafer as well as serving its primary purpose of inducing resonance vibrations in the form of standing waves into the wafer (Fig. 2.13).

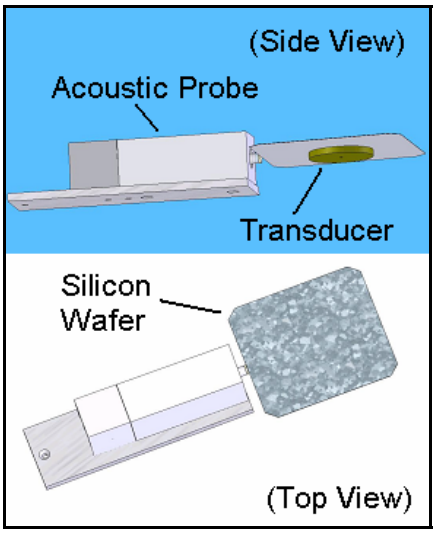

Figure 2.13 Mutual Layout of the Transducer, Wafer, and Probe in the RUV Setup.

Vacuum pressure is monitored with an inline vacuum gauge. The need for the vacuum gauge is twofold. First, when a wafer does not establish firm vacuum coupling with the transducer measurements can be inaccurate. A vacuum gauge allows a signal to be sent to the user indicating a bad vacuum and the measurement can be aborted. The vacuum gauge is also needed to monitor the vacuum pressure being applied to the wafer. Vacuum pressure from the transducer results in stress on the wafer which can shift RUV parameters as seen in figure 2.14 for the 200 microns thick Cz-Si wafer (is this correct?). This pressure effect is even more pronounced in thinner wafers of ~100 microns

thickness. This effect, of upward peak shift and broadening, is consistent with RUV diagnostics of elastic stress in EFG polycrystalline Silicon wafers [38].

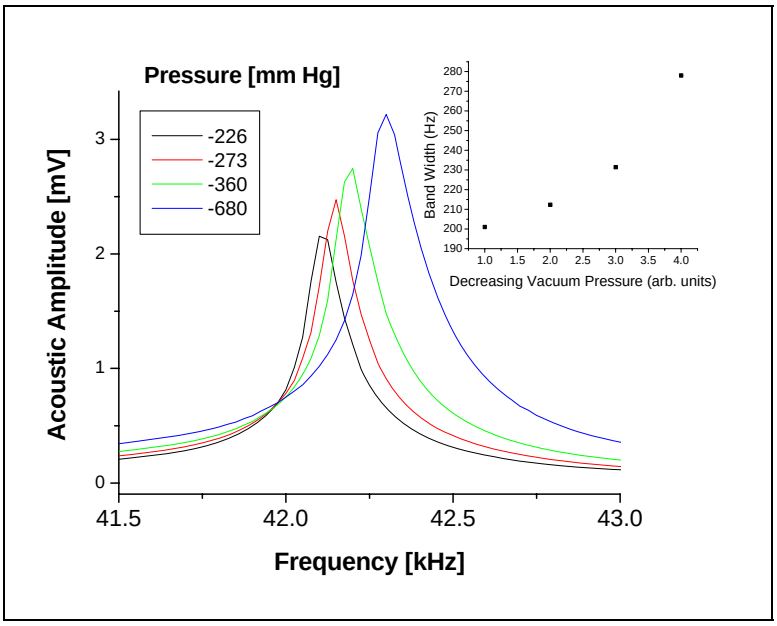

Figure 2.14 RUV Parameter Shift Due to Increasing Vacuum Pressure Through Transducer, as Monitored by the In-line Vacuum Gauge Indicating Negative Pressure Created Between Transducer and Silicon Wafer. Insert Shows Broadening Bandwidth with Increasing Stress from Greater Vacuum Pressure.

The acoustic probe transmits the electrical signal to a computer controlled lock-in amplifier allowing detection of mV scale ultrasonic signals with sufficient signal-to-noise ratio. In our experiments the wafer was excited with longitudinal vibrations that were detected by the acoustic probe for further analysis. Full automation of the measurement procedure was implemented in order to have a platform for making time sensitive adjustments to reduce the complete RUV measurement time. Through the use of a vertical stage for wafer loading and unloading as well as a horizontal stage for probe contact force control and a computer controlled vacuum valve, numerous repetitive

measurements could be taken. Valuable data regarding repeat measurement uniformity on a single wafer as well as among a group of wafers was available with the automated setup.

2.4 Sample Description

The photovoltaic industry's adoption of square shaped wafers in order to maximize cell coverage on solar panels guided our experiments to using square shaped wafers and cells of industry standard sizes. Pre-processed silicon wafers from various vendors came in three primary sizes: 103 mm x 103 mm (Isofoton, HCT), 125 mm x 125 mm (BP Solar), and 156 mm x 156 mm (Q-cells). Polycrystalline cast silicon and Cz-Si single crystalline wafers were the primarily used sample materials in this study. Wafer thickness varied from 100 μm to over 300 μm. Most of the study was carried out on Cz-Si and cast Poly-Si chemically etched wafers, before phosphorous diffusion, anti-reflecting coatings and front/back contact depositions, but after saw introduced surface damage had been etched off. Data on complete solar cells as well as semi-processed cells is not included in this thesis, yet future work may proceed in this direction.

Chapter Three: Experiments and Results

Physical systems can be characterized by their unique reaction to stimuli. Systems respond to cyclical stimuli of different frequencies in unique ways. A vibrating system may have certain mechanical characteristics, such as stiffness, size, shape, etc., that make it more responsive to stimuli at specific frequencies. The specific frequencies under which the system is most excitable are coined 'resonance frequencies'. Most physical systems have numerous frequencies at which physical response is greater than at slightly different frequencies. These individual resonance frequencies are termed modes. These resonance mode frequencies, as previously mentioned, are dependent on the physical characteristics of the body under measurement. Changes in the system, such as cracks, cause shifts in the resonance frequencies. We explored the characteristic resonance modes for square shaped silicon wafers for use in PV applications.

3.1 RUV Mode Identification

Specific resonance vibration modes were found by first measuring a full spectrum frequency scan on the representative cast and Cz-Si wafers with an illustrative example presented in Figure 3.1 for a 156 mm x 156 mm cast Si wafer. RUV in numerous square-

shaped wafers of different sizes, accepted as photovoltaic industry standards, were measured and their average peak positions are summarized in Table 3.1.

Table 3.1 Experimental (a) and FEA Calculated (b) Resonance Peak Frequencies for 4 Vibration Modes in Si Wafers of Different Size. Calculated Frequencies are Rounded to the Last Digit.

Mode #	1		2		3		4	
	Peak Modal Frequencies (kHz)							
Wafer Size [mm]	(a)	(b)	(a)	(b)	(a)	(b)	(a)	(b)
103x103	42.5	47.65	69.85	69.64	-	103.13	-	135.31
125x125	37.3	39.26	57.42	57.38	83.85	84.98	-	111.49
156x156	29.7	31.46	45.67	45.98	68.17	68.09	87.45	89.34

Each experimental peak represents a particular vibration mode that is compared with FEA results. FEA analysis was carried out using the ANSYS 8.0 program package with the help of Mr. Oleg Polupan. FEA parameters for analysis included a size specific mesh with square-shaped 1 mm or 2 mm individual elements. The silicon wafer is modeled as an isotropic thin plate with a Young's modulus of 167 GPa, a Poisson ratio of 0.3, and a density of 2.3×10^3 kg/m^3. Free vibrations of the plate were calculated neglecting the effect of the transducer coupling and acoustic probe contact. Even in this simplified model, we found a close match of the experimental and calculated frequencies (Table 3.1) in wafers of different sizes.

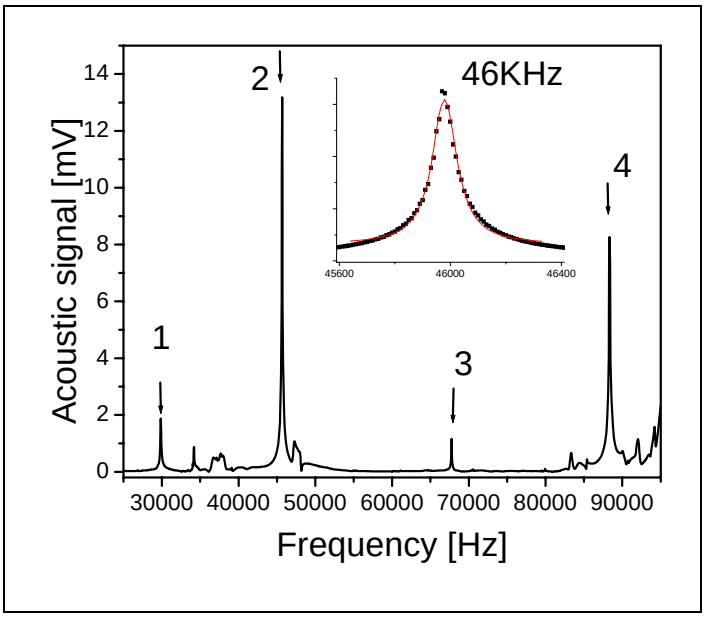

Figure 3.1 Full Frequency Scan on 156mm x 156mm Cast Si Wafer. Arrows Show Four Individual RUV Modes. Insert Zooms on the #2 Mode at 46 kHz (Points) with Lorentzian Fit (Solid line).

As vibration theory predicts, the resonance frequency of a specific mode (f_{res}) shifts upwards with reducing the wafer area (a). It practically obeys a simple relation, such as $f_{res} \sim a^{-1}$ which is illustrated in Figure 3.2 in the case of the four vibration modes numbered in Figure 3.1

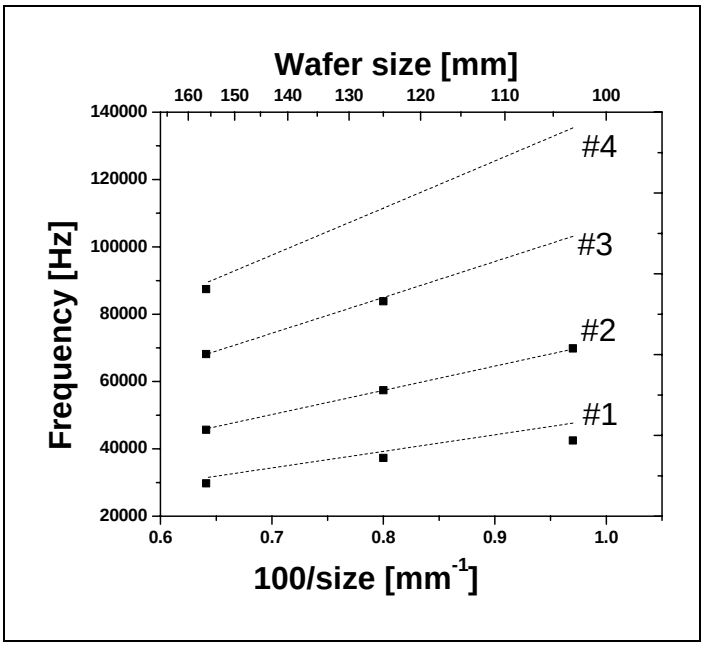

Figure 3.2 Variation of the Resonance Peak Position Versus Edge Length of the Square Shaped Wafer. Dotted Lines – FEA Calculations, Dots – Experimental Data on Si Wafers.

In Figure 3.3 (a-d) we present FEA mode shapes for resonance vibrations indicated by arrows and numbers in Figure 3.1. Following closely with the experimental and calculated resonance frequencies as seen in Table 3.1 we are confident with this mode identification. To further verify this and in order to assure that FEA modeling matches the experimental data and to provide correct representation of the vibration modes we conducted an experiment to determine the mode shape from a series of amplitude measurements along a wafer's edge. Once the peak vibration frequency of a specific mode was found, the mode shape was analyzed by conducting a single peak scan along one edge of the symmetrical wafer. The amplitude changes from point to point were consistent with peaks and nodes in the modal standing waveform. The resonance peaks were measured with a step size between 3 and 5 mm, depending on wafer size (a),

to construct a representative mode shape. The change in peak amplitude along the edge of the vibrating wafer was found to be similar to the mode shapes at the respective frequency as predicted by FEA.

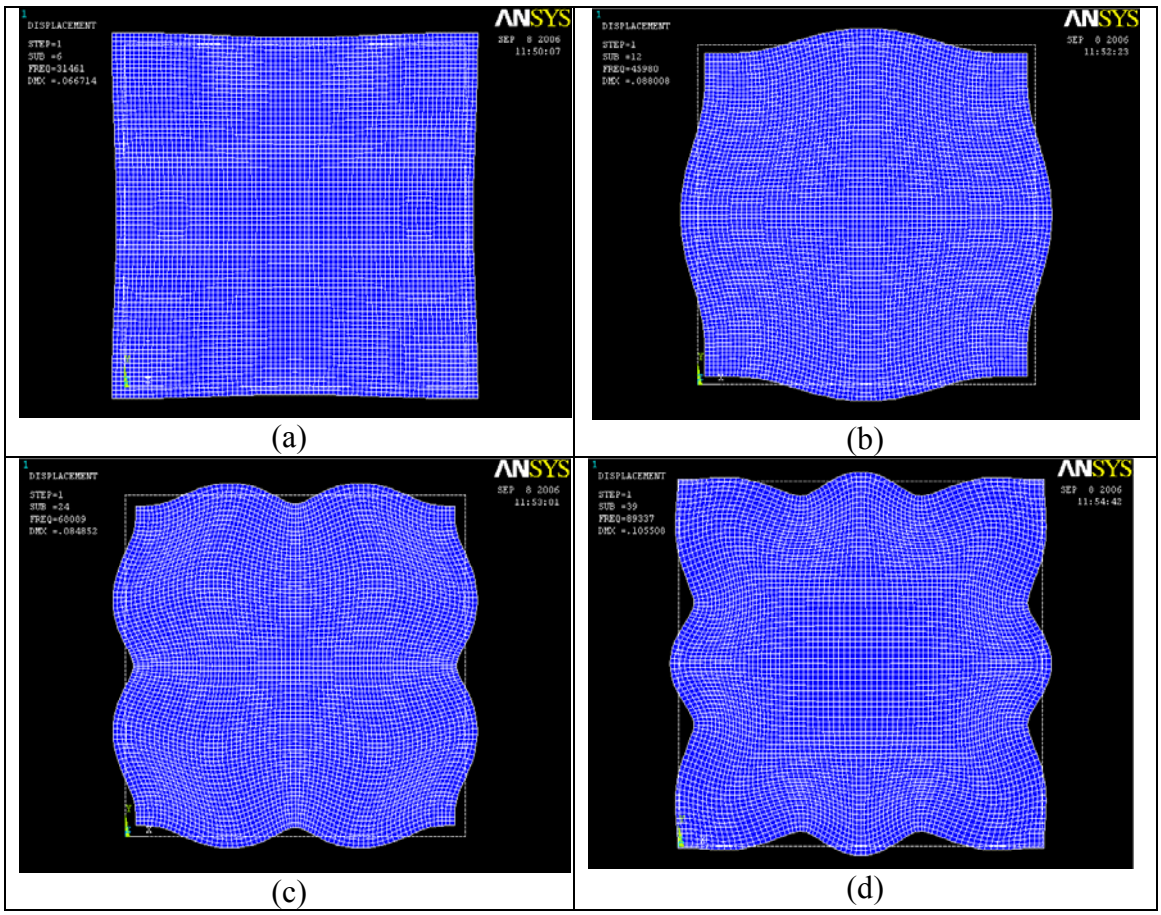

Figure 3.3 (a-d) FEA Calculated Mode Shapes Corresponding to Peaks 1-4 Respectively as Seen in Figure 3.1.

Two unique resonant modes were analyzed at approximately 31.5 kHz and 46 kHz, corresponding to peaks #1 and #2 respectively in Figure 3.1 for a 156 mm x 156 mm square shaped cast silicon wafer. Figure 3.4 shows the correlation between the amplitudes of the experimental data and theoretical FEA results. Experimental edge scans on the other two vibration modes, #3 and #4, also showed close relevance to calculated

edge scans. Specifically, the number of vibration nodes matches for both of the modes. However, accurate fit of the experimental data is complicated due to a larger number of vibration periods for these high-frequency modes. Good correlation validates using the FEA modeling as a guideline for crack influenced frequency-shifting behavior (see below). The slight asymmetry seen in figure 3.4 can be explained by the non-uniformity of the transducer. Our tests have shown slightly higher peak amplitude created by the left side of the transducer in all cases of wafer orientation.

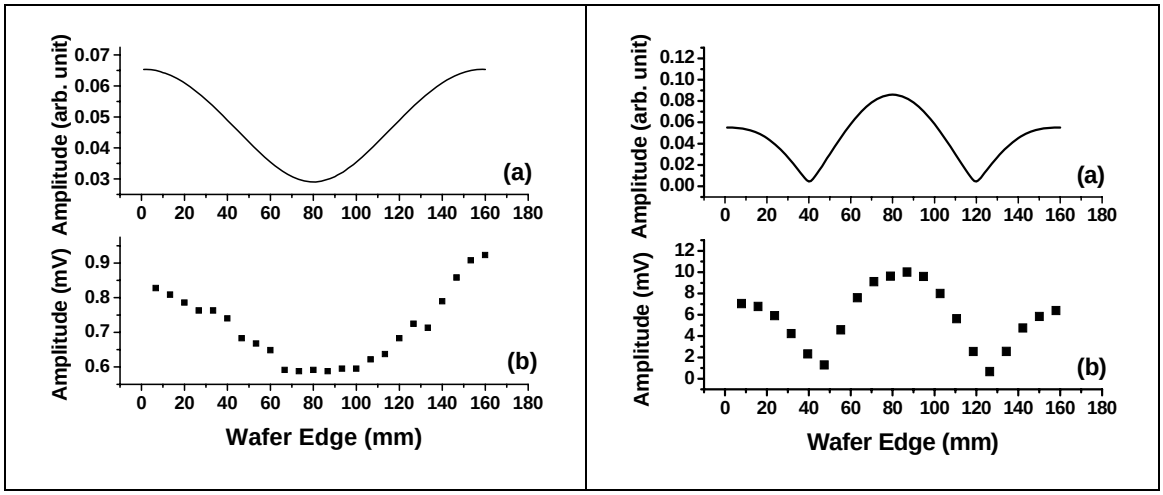

Figure 3.4 Amplitude Variation of the RUV Mode along the Wafer Edge Representing Peak 1 at 30 kHz (left) and Peak 2 at 45 KHz (right). (a) FEA Modeling, (b) Experimental Data.

In a study on reconstructing physical mode shapes from edge scans, the four sides of the wafer were all measured at each of the four individual peaks as noted in figure 3.1. A rough image reconstruction was done of the four wafer edges for each mode and can be seen in figure 3.5. Although our FEA modeling gives us a starting point for how the mode shapes should look, many physical variables, including probe or transducer contact,

come in to play and slightly alter these results. A comparison of the FEA results along side the physical results is presented in figure 3.5.

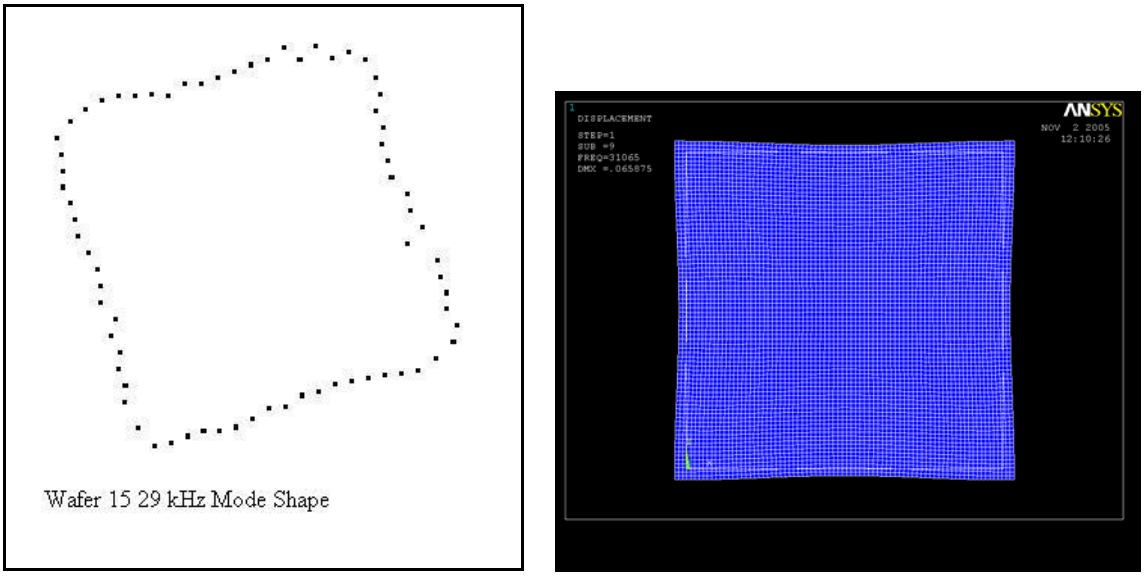

(a)

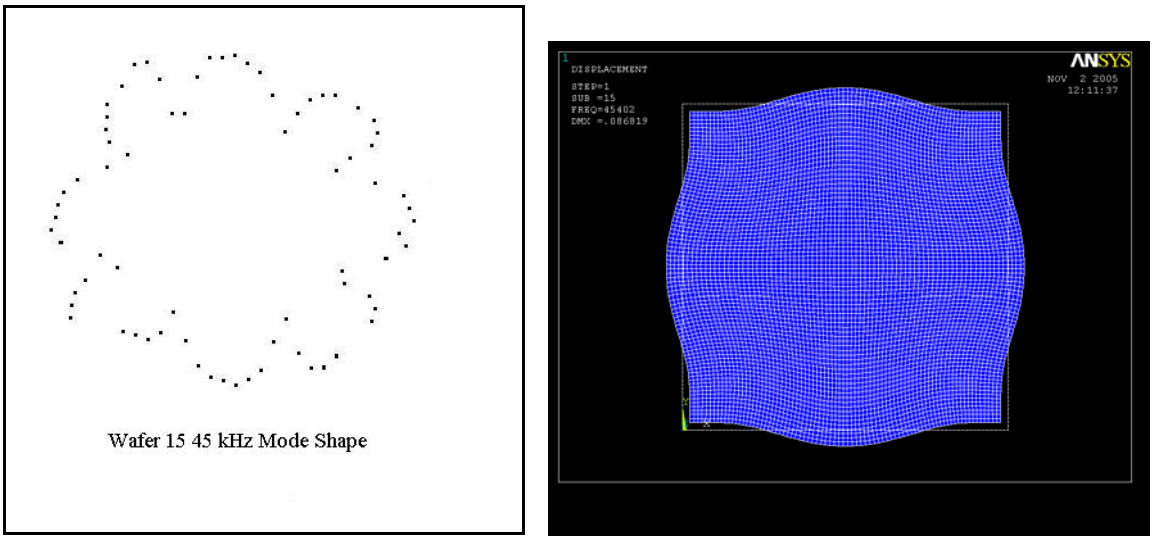

(b)

Figure 3.5 (a) 30 kHz, (b) 45 kHz, (c) 67 kHz, and (d) 87 kHz Physical Mode Shape Reconstruction Comparison to FEA Results.

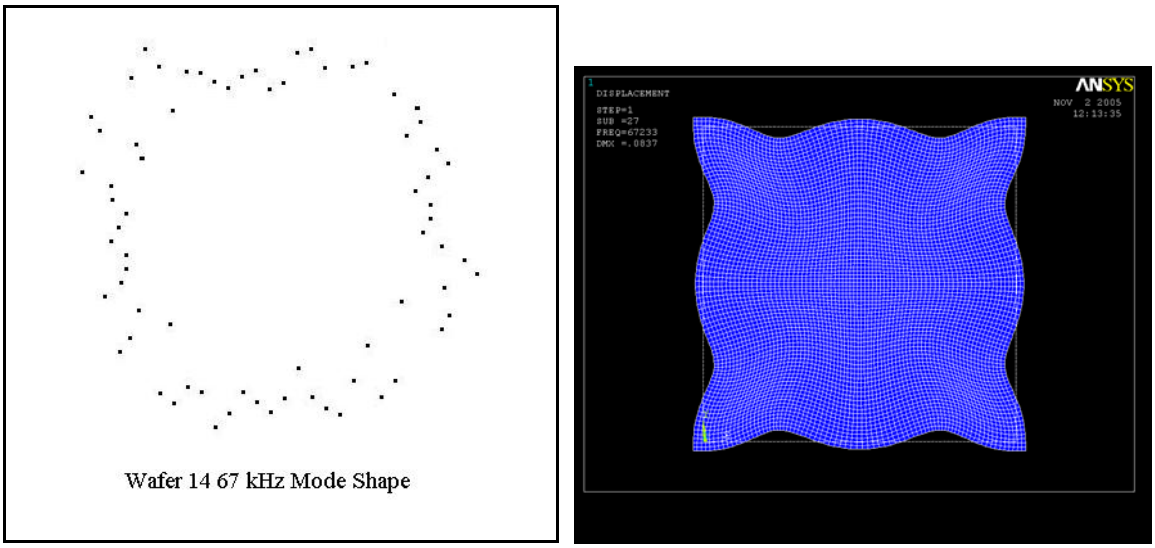

(c)

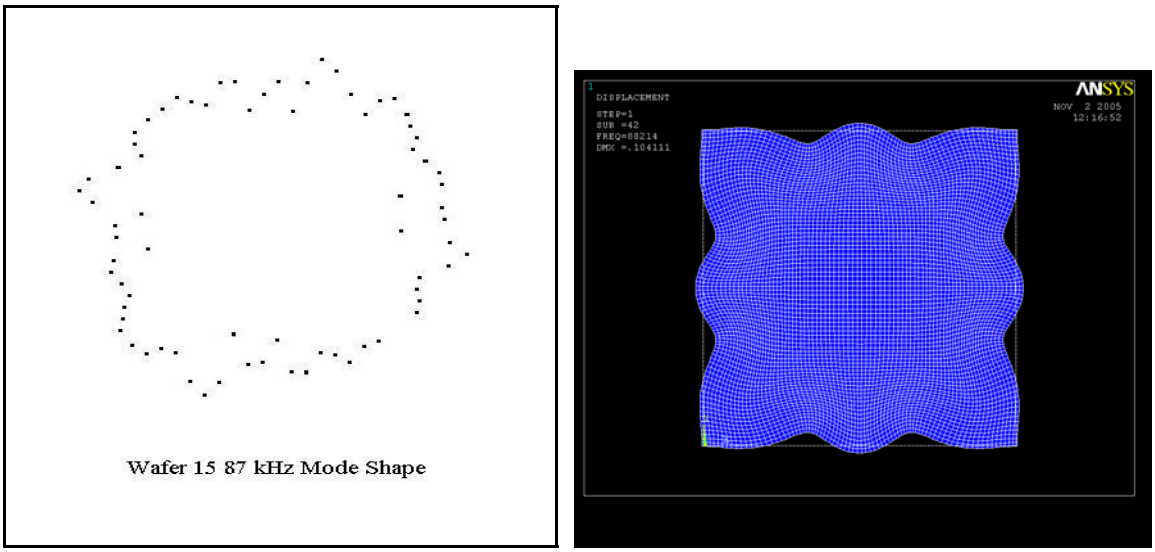

(d)

Figure 3.5 (a) 30 kHz, (b) 45 kHz, (c) 67 kHz, and (d) 87 kHz Physical Mode Shape Reconstruction Comparison to FEA Results.

3.2 RUV Crack Detection

3.2.1 Crack Engineering

Due to the fact that finding naturally occurring cracks with the precise position and length necessary for analysis is nearly impossible, cracks were intentionally introduced into the (100) oriented Cz-Si wafer. This was achieved by pressurizing the wafer near the edge at the intended crack location with a diamond tipped scribe. Consistently increasing the pressure until a cracking sound was heard usually achieved the desired results (Figure 3.6). Because of the possibility for crack propagation in either of two cleavage crystallographic <110> directions the crack had to be coaxed to propagate in the required direction in cases where specific crack location studies were being conducted. This could generally be achieved by scratching (mm-length) the wafer surface along the intended propagation direction and then pressurizing the wafer edge at the damage location with the diamond scribe. The directional surface damage effectively lowers the surface energy, $\gamma_{s,}$ leading the crack in the intended direction in an energy favorable decision. Crack making without initial directional forcing damage was often used due to its ease and lack of extra wafer damage from scribing.

Engineered cracks typically appeared as singular cracks in either 'left' or 'right' crystal directions or as dual cracks heading in both directions simultaneously from the point of pressurization. Crack elongation can be achieved by finding the tip of the initial crack and slightly pressurizing it with the diamond scribe. In brittle materials this can unfortunately also lead to crack "branching" as illustrated in Figure 3.6c and discussed by the authors in [10]. To avoid this undesirable effect a consistent crack elongation without

'branching' cracks can be achieved by precise pressurizing at the crack tip as seen in figures 3.6e and 3.6f. A crack elongation machine was fabricated after a similar machine of the authors in [37] and is presented in section 3.3.

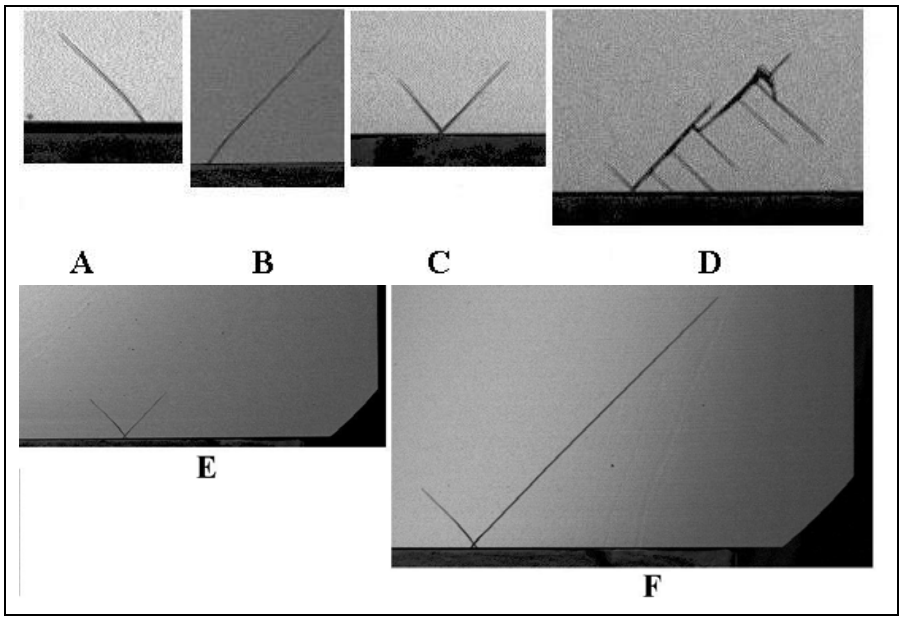

Figure 3.6 Possible Crack Propagation Directions (a) and (b) Single (c) Dual (d) Branched and Correct Elongation Procedure (e) Wafer with Initial Induced Crack (f) Same Wafer after Successful Elongation.

3.2.2 Experimental Crack Detection

Through the use of FEA analysis we have begun to understand the apparent selective sensitivity of certain RUV modes to periphery cracks. It was initially expected that different modal frequencies would have different responses to cracks at different positions in the wafer. Based on this hypothesis, experiments were carried out using Cz-Si wafers to determine the sensitivity of the RUV system to cracks originating from the

edge center. Cz-Si wafers were used in this study primarily due to their low internal stress, less than 1 MPa, when compared to polycrystalline Si wafers where average stress can vary and average 10MPa and peak stress one order of magnitude higher [38]. It can be seen (figure 3.7) that at this particular crack position the Peak # 2 mode is less sensitive to the 6 mm central crack with a small downward frequency shift of 18 Hz, negligible bandwidth broadening and only a slight reduction in amplitude (0.2 mV). In comparison, the Peak #3 mode shows a substantial downward frequency shift of 655 Hz along with the amplitude reduction of 1.7 mV and bandwidth increasing by 40 Hz for the same wafer and same crack.

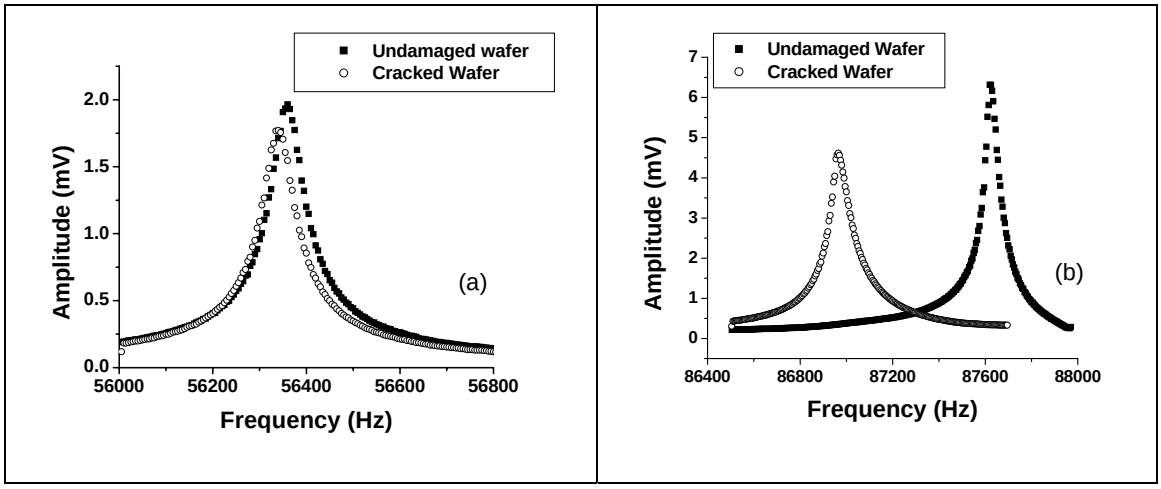

Figure 3.7 (a) Peak #2 Mode Showing a small, 18Hz RUV Peak Shift when 6 mm Crack was Introduced to the Wafer's Edge (b) Peak #3 Mode Showing Larger, 655Hz Peak Shift on Same Cracked Wafer.

This experimental data was compared with FEA analyses. The model crack was located at the wafer center at 45^0 with respect to the wafer edge, similar to the experiment. Crack length was changed from 1 mm to 16 mm and peak position was

calculated for vibration modes at 40, 58 and 86 kHz (mode numbers 1, 2 and 3 in Figure 3.1). The results presented in Figure 3.8a illustrate that in the case of a central crack, a shift of the mode #3 with highest frequency of 86 kHz is the largest, which is consistent with the experimental data in Figure 3.7. To improve the quantitative consistency of the calculations with the experiment, we introduced in the FEA model spring elements with variable stiffness. These elements connect the two planes of the crack and model the effect of vibration damping of the wafer due to the crack. Increasing stiffness reduced the peak shift as presented in Figure 3.8b for the 10mm central crack. This fitting parameter better matches the experimental RUV data with FEA modeling.

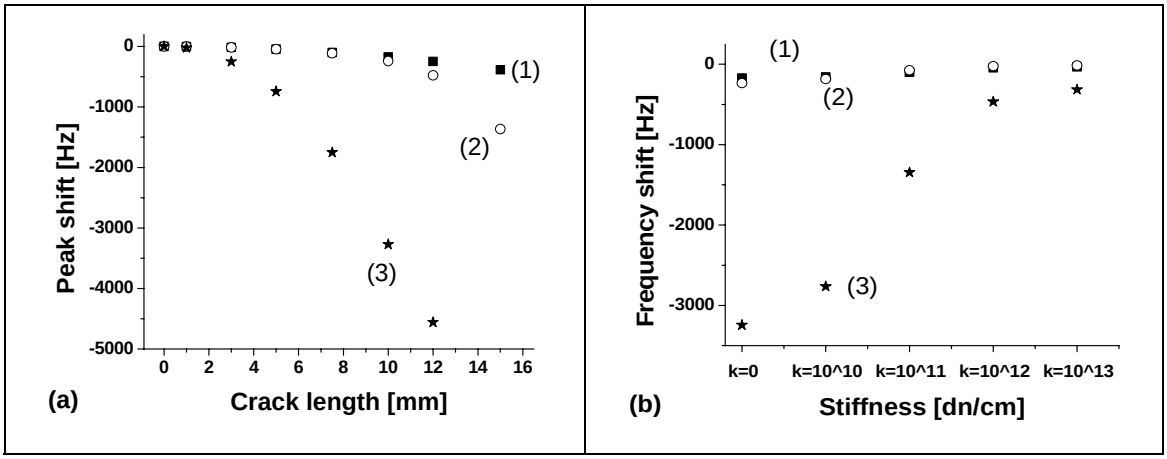

Figure 3.8 (a) Peak Shift Versus Crack Length Dependences for Three Vibration Modes on 125mm Wafer for the Center Edge Crack Location; (b) Variation of the Peak Shift with Stiffness of the Spring Element. (1) Mode #1 (40 kHz), (2) Mode #2 (58 kHz), and (3) Mode #3 (86 kHz). Notice that Mode Frequencies are Scaled up due to Reduced Wafer Size.

We also observed using the FEA modeling that the crack location along the wafer's edge plays a significant part in the resonance vibration response. In Figure 3.9 this fact is documented as a peak shift versus crack length in two different crack positions

along the edge of the 125mm x 125mm wafer, at the edge center and at the corner. Three different vibration modes show different sensitivity with respect to the crack location. Specifically, mode #3 shows the largest peak shift at the center crack location (Figure 3.9a) and the mode #2 when the crack is located at the corner (Figure 3.9b). This interesting feature can further improve crack detection sensitivity by tracking the RUV parameters of different vibration modes to minimize the probability of passing a cracked wafer through the production line.

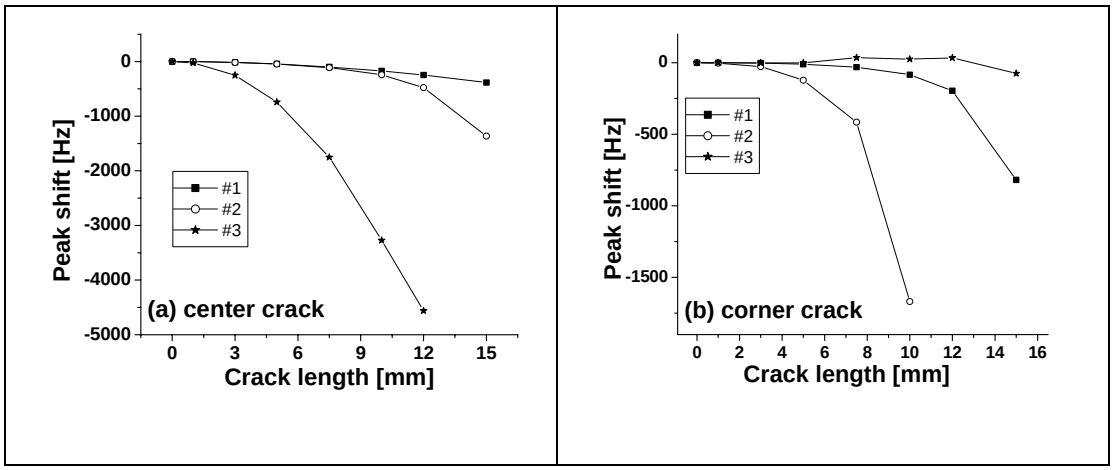

Figure 3.9 (a) FEA Calculated Variation of the Peak Position Versus Crack Length to a Center Crack Position for Vibration Modes #1, #2, and #3 (b) Same for a Crack at the Corner Position.

RUV measurements were done on several wafers with cracks located at one of the corners of the wafer to investigate the reaction of the RUV parameters. The FEA predicted that the #2 mode would be more sensitive to cracks located in the corner of the wafer rather than the center. Our results show that the predicted corner crack position does modify the vibratory modal shape at the #2 peak more than the other peaks as shown in figure 3.10. The number two mode shifted to a lower frequency by 55 Hz and the

number three mode shifted by 20 Hz for the corner crack position. This shift was from a relatively short 5 mm crack and the effect is greater for longer crack lengths as specified on the SAM image on Figure 3.11.

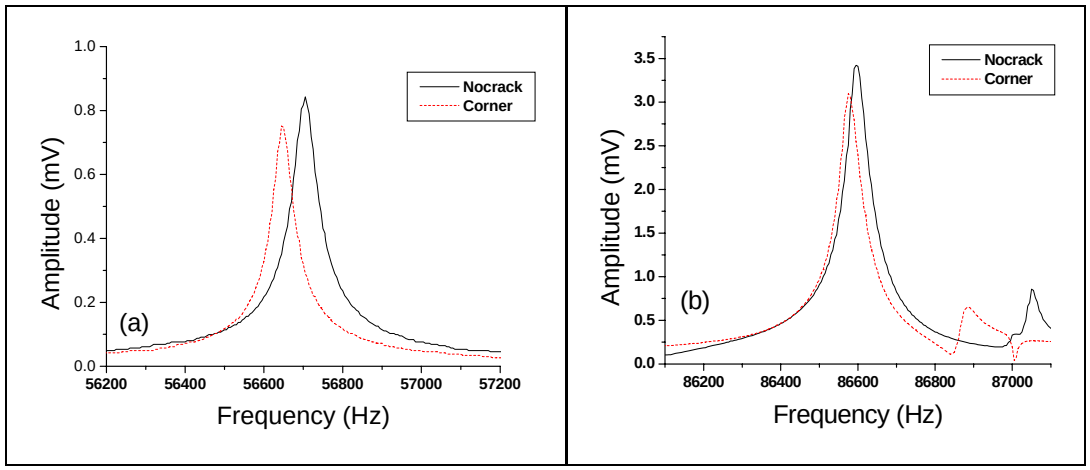

Figure 3.10 RUV Peak Shift from a 5mm Corner Crack Measured for (a) #2 and (b) #3 Frequency Modes. Notice that #2 Mode shows 55Hz Downward Shift of the Resonance Frequency compared to 19Hz Shift of the #3 Mode.

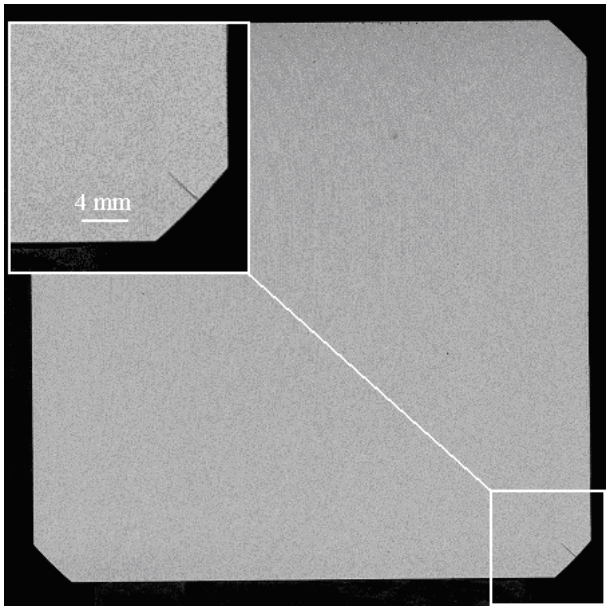

Figure 3.11 4 mm Corner Crack in Wafer 34A Contributing to the Shift of the # 3 Peak.

3.2.3 Cracks on Production Grade Wafers

RUV analysis was conducted on a set of identical in size 125 mm x 125 mm production grade cast wafers with results presented in Figure 3.12. This sequential RUV data collection and analyses is in close relevance to the solar cell testing routine targeting to reject mechanically unstable Si wafers in PV production. Three parameters of the RUV peak were analyzed: peak position, peak bandwidth and peak amplitude. One of the wafers (# 11) was clearly an outlier versus the other wafers. Using SAM measurements we confirmed that this wafer had a 10 mm periphery crack which was clearly observed in the RUV testing.

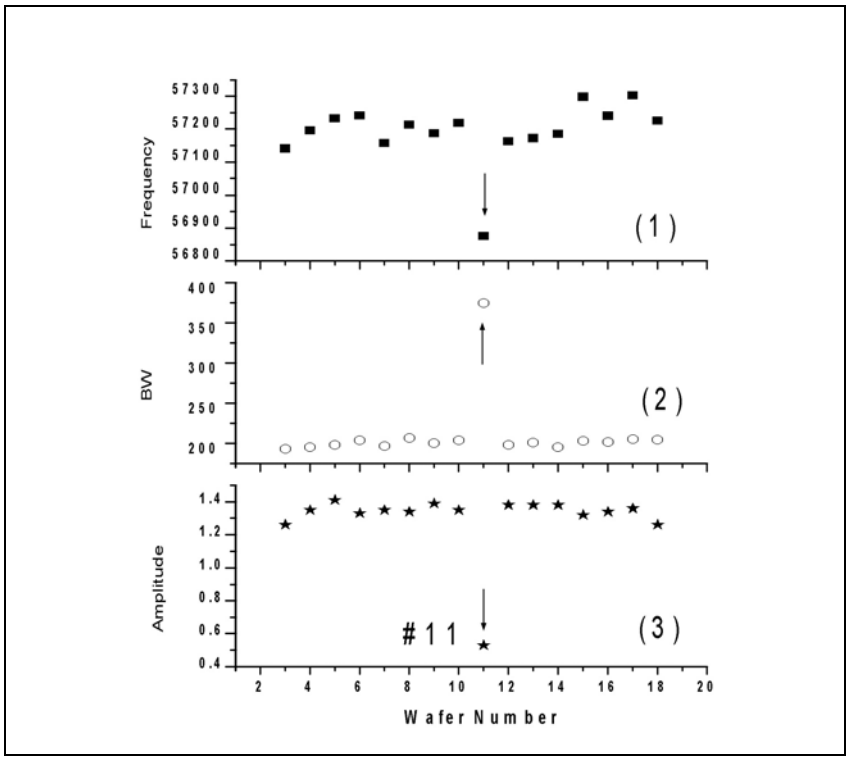

Figure 3.12 Crack Detection Run on a Set of 125mm x 125mm Cast Wafers with Wafer #11 Possessing 10 mm Periphery Crack Identified by RUV Parameter Variations (1) Peak Position, (2) Peak Bandwidth, and (3) Peak Amplitude.

Numerous similar experiments have been conducted with uniform wafers from a vendor to act as sampling tests as would be found in a manufacturing situation. One such experiment is documented in figure 3.13. A set of 200 um thick 100mm x 100mm Cz-Si wafers were measured as delivered from a vendor and wafer #39 was found to show shifted RUV parameters as seen in figure 3.13. Further analysis under the SAM revealed a periphery crack as seen in figure 3.14. These experiments further validate the RUV techniques potential for in-line photovoltaic wafer crack detection.

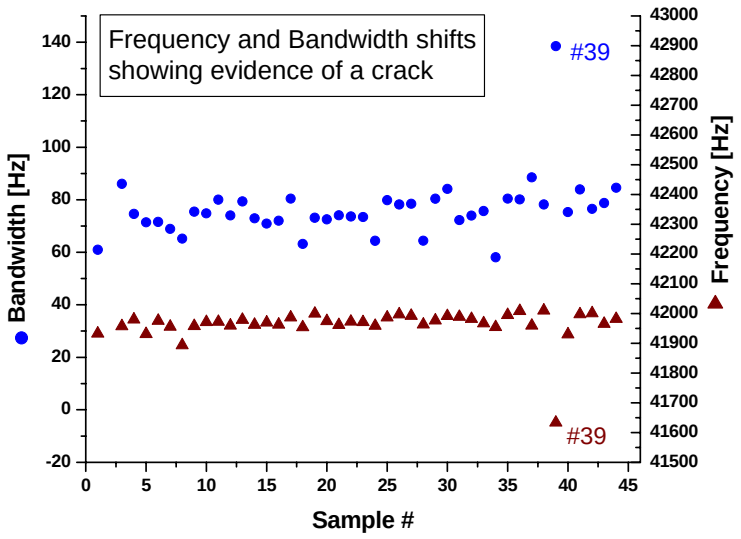

Figure 3.13 Sample of 200um Thick Cz-Si Wafers as Delivered from Vendor. Wafer 39 Clearly Shows Shifted Bandwidth and Frequency, Indicating a Crack.

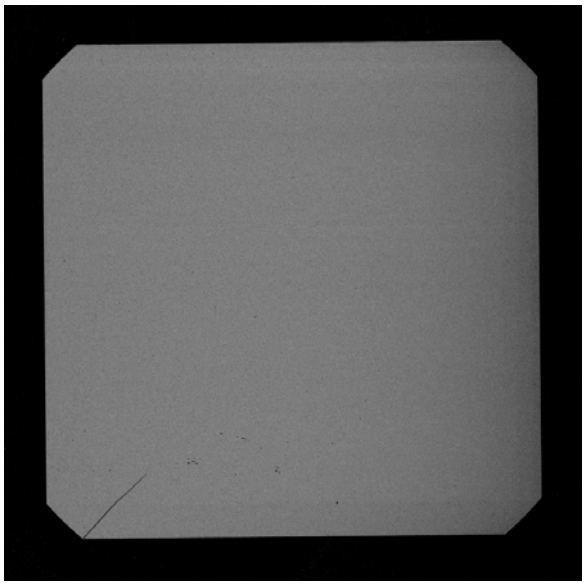

Figure 3.14 Crack in Wafer 39 as Detected by the RUV System and Imaged Here Using the Sonix SAM.

3.3 Crack Elongation Apparatus

The study of fracture in brittle silicon is especially difficult due to the cleaving nature of the material. Cleavage along precise crystal directions is known to be difficult to accurately control [12]. Specific alignment of the wafer under test is crucial to achieving any results. A crack elongation apparatus was built modeled after the system used for GaAs cleavage experiments in [37]. The system consisted of a clamping plate and a pushing rod attached to a z-stage stepper motor which was computer controlled. The wafer was oriented at a diagonal so that the clamping plate aligned with the <110> direction of intended cleavage as in figure 3.15.

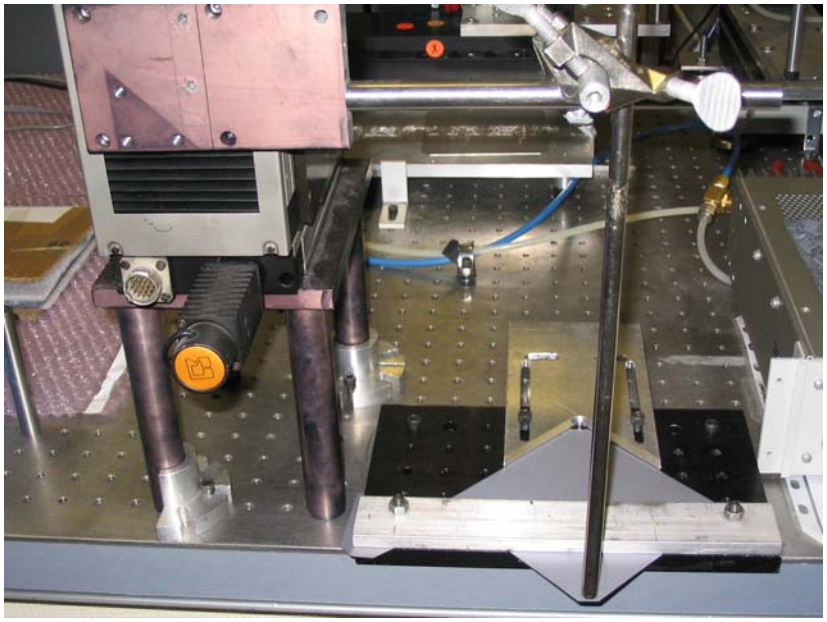

Figure 3.15 Crack Elongation Apparatus Showing 125 mm x 125 mm Cz-Si Wafer in Clamping Apparatus with Pushing Rod, Attached to Z-stage, at the Wafer Corner.

Initial experiments were conducted on wafers prior to any known damage. Wafers without damage showed bending strengths correlating to z-stage displacements of over 4 mm of deflection. Undamaged wafers were bent in increments of .5mm and measured on the RUV system to look for peak shifting and the SAM. Initially single pushes were used and later multiple pushes at the same deflection were done. No wafer in our tests had a crack originate from these bending tests although there were numerous fractures.

The initial intent of the machine was to study the effects of the RUV parameters with respect to increases in crack length. Wafers were first placed into the clamping plate and aligned. The wafers were then marked along the crystal plane in which the crack was to be introduced. Cracks were introduced using the previously described method. Pushing experiments were done to try to elongate the cracks. The RUV system was

sensitive to changes after the elongation attempts but no significant elongation of the crack could be seen in the SAM in most cases. This was likely due to an opening of the crack rather than a strict elongation. Success was achieved in the case of one wafer in which a 13 mm dual crack was extended along one direction to over 60 mm as shown in Figure 3.16.

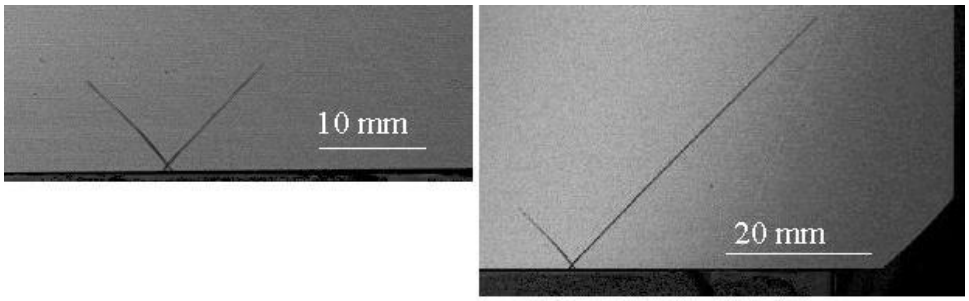

(a) **(b)**

Figure 3.16 Successful Elongation of Wafer Using Crack Elongation Machine.

3.4 Liquid Evaporation Crack Detection Method

An effect noticed during routine experiment that may prove useful is described. When removing wafers from the DI water bath used in the SAM, occasionally water seemed to evaporate last at the site of cracks. After the initial discovery of this technique further effort was instilled to examine the conditions under which this effect occurred. The wafer must have no surface film, marks, or smudges at the area of the crack that water could cling to. Also, the evaporation process was examined. If the water on the cracked wafer was allowed to naturally evaporate it was often the case that the water would evaporate first from around the edges and last at the center leaving no image of the crack. If the wafer was wiped dry, leaving a very thin layer of water over the surface, evaporation would occur in a more uniform manner around the crack often leading to an

image of the crack in water. Other liquids were tried including acetone and methanol. Neither of which showed the effect. This may be to the larger size of these molecules when compared to water. This method is not fully developed and is inconsistent in terms of achieving repeatable results. Numerous attempts at documenting this effect have failed due to its inconsistent nature. This effect was used to determine where cracks existed in known cracked wafers for elongation attempts.

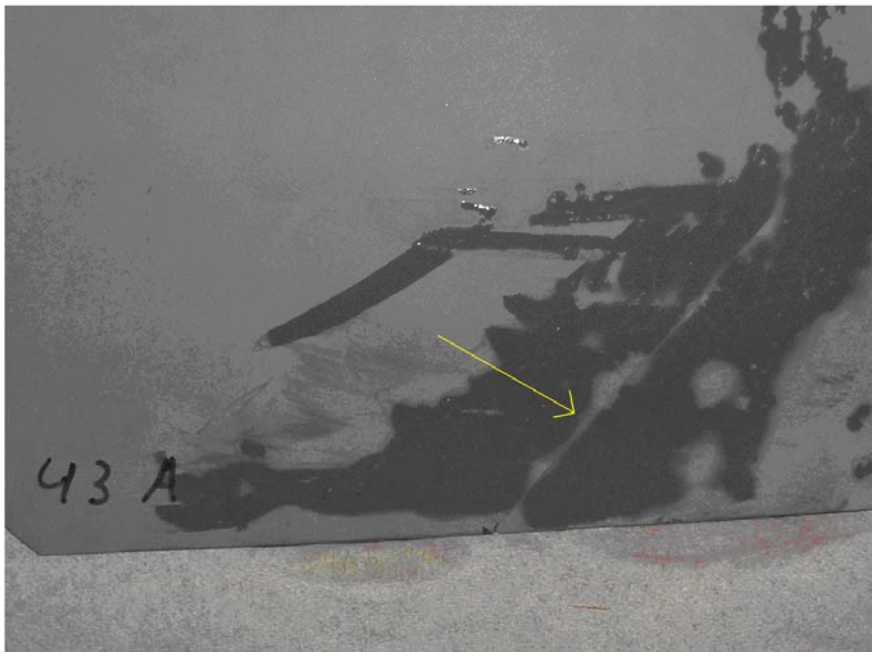

Figure 3.17 Photo of Water Evaporation Around 20 mm Crack.

Chapter 4: Conclusions and Recommendations

The work presented in this thesis addresses a critical need of the photovoltaic industry for non-destructive crack detection methodology applicable for production-grade silicon wafers and solar cells. The evolution of the experimental RUV system for use as a crack detection unit was motivated by the current needs of the photovoltaic industry. The development of the RUV system for accurate crack detection along with the study of the defining parameters of the system was achieved during the time of the research. New experimental modifications were employed to advance sensitivity of the RUV method for crack detection including:

- Simultaneous tracking of the resonance frequency, bandwidth, and amplitude to reveal the effect of cracks on the RUV peak
- Sensor control of contact force between the wafer and acoustic probe
- incorporation of a visco-elastic CMP element on the tip of the acoustic probe
- addition of a spring behind the probe for controllable wafer-probe contact force
- advances in wafer handling and alignment through the use of newly designed stages and holders allowing the use of the three primary sized PV silicon wafers with no adjustments necessary when going between sizes
- vacuum pressure monitoring
- important addition of wafer edge scanning capabilities

A further understanding of the RUV parameters reaction to cracks was attained through several key experiments including:

- Edge scan experiments showing physical mode shapes relating to FEA modeling
- Large sample set runs through the RUV system showing accuracy in fast crack detection, validated by use in two industrial settings.
- Crack location experiments giving insight into specific RUV mode sensitivity to certain crack positions.
- FEA modeling showing similar results for specific RUV mode sensitivity to crack location.

The research completed during the timeframe of this thesis has been instrumental in the advancement of the RUV technique for crack detection. The dependability of the notable shift in RUV parameters in the presence of a crack including, amplitude, bandwidth, and frequency, allows the system to quickly detect cracked wafers. The additions and advancements on the system described here within have increased the techniques sensitivity to cracks as well as increased the competence in the technique and given understanding to the RUV parameters reaction to variables in the system and among wafers. The RUV approach to crack detection is a viable method for potential use in industry as shown by funding of the program by industrial partners (RWE Scott Solar, BP Solar) and building of a prototype of the RUV crack detection machine at the NNRC spectroscopy laboratory at USF.

Future work to improve the RUV system would consist of reproducibility studies on large sets of both cast and EFG polycrystalline wafers with possible incorporation of a

statistical algorithm to determine good and bad wafers. Work on system stability on the same wafer over numerous measurements over a period of days allowing all environmental factors to change would benefit system reliability. Important issues still need to be resolved in relation to the full measurement time. This includes closely monitoring the effects of changing the lock-in time constant as well as efficient program execution. Future study of the effect of crack position and length could be modeled for many more crack positions using FEA analysis. Further work is necessary on the RUV system before it can comfortably be incorporated into a wafer manufacturing facility.

The results presented in this thesis were published in the following articles and conference proceedings:

1. *William Dallas*, Oleg Polupan and Sergei Ostapenko, "Resonance Ultrasonic Vibrations for Crack Detection in Photovoltaic Silicon Wafers ", Sem. Sci. Technology, in press

2. A. Belyaev, O. Polupan, *W. Dallas*, S. Ostapenko, and D. Hess "Crack detection and analyses using resonance ultrasonic vibrations in full-size crystalline silicon wafers" Appl. Phys. Lett. 88, 111907 (2006)

3. Sergei Ostapenko, *William Dallas*, Oleg Polupan, John Wohlgemuth, "Resonance Ultrasonic Vibrations for Crack Detection in PV Crystalline Silicon Wafers" 26th IEEE World Conference on Photovoltaic Energy Conversion (WCPEC-4), Hawaii, 2006

4. *W. Dallas*, O. Polupan, S. Ostapenko, "Resonance Ultrasonic Vibrations for Crack Detection in PV Crystalline Silicon Wafers" 16th Workshop on Crystalline Silicon Solar Cells and Modules: Materials and Processes (NREL) Denver, Colorado, August 6–9, 2006

5. A. Belyaev, O. Polupan, *W. Dallas*, S. Ostapenko, D. Hess, J. Wohlgemuth, "Crack Detection and Analyses Using Resonance Ultrasonic Vibrations in Full-Size Crystalline Silicon Wafers" Solid State Phenomena, (2005) 108-109, 509-514

6. A. Belyaev, *W. Dallas*, O. Polupan, L. Zhukov, S. Ostapenko, "Resonance Ultrasonic Vibrations (RUV) for Crack Detection in PV Crystalline Silicon" 15th Workshop on Crystalline Silicon Solar Cells and Modules: Materials and Processes (NREL) Vail, Colorado ,August 7–10, 2005

References

1. Kasap, S.O., *Principles of Electronic Materials and Devices.* 2nd ed. 2002: McGraw Hill. 68.

2. Goetzberger, A., J. Knobloch, and B. Voss, *Crystalline Silicon Solar Cells.* 1998: John Wiley & Sons, Inc. 136-137.

3. Schmidt, J., A.G. Aberle, and R. Hezel. *Investigation of Carrier Lifetime Instabilities in CZ-grown Silicon.* in *26th IEEE Photovoltaics Specialists Conference.* 1997. Anaheim, CA.

4. Keck, P.H. and M.J.E. Golay, *Crystallization of silicon from a floating liquid zone.* Phys. Rev., 1953. 89: p. 1297.

5. Shimura, F., *Semiconductor SIlicon Crystal Technology*. 1989: Academic Press, Inc. 128.

6. Kalejs, J.P. *An overview of new developments in crystalline silicon ribbon material technology for solar cells*. in 3rd World Conference on Photovoltaic Energy Conversion. 2003. Osaka, Japan.

7. Wronski, C.R., et al. *Progress in amorphous silicon based solar cell technology*. in RIO 02 - World Climate & Energy Event. 2002. Rio de Janeiro, Brazil.

8. Winer, K., *Defect formation in a-Si:H.* Physical Review B, 1990. 41(17): p. 12150.

9. Staebler, D. and C.R. Wronski, *Reversible conductivity changes in discharge-produced amorphous Si.* Applied Physics Letters, 1977. 31(4): p. 292.

10. Anderson, T.L., *Fracture Mechanics Fundamentals and Applications*. 2nd ed. 1995: CRC Press, Inc. 39,282.

11. Perez, R. and P. Gumbsch, *Directional anisotropy in the cleavage fracture of silicon.* Physical Review Letters, 2000. 84(23): p. 5347-5350.

12. Hauch, J.A., et al., *Dynamic fracture in single crystal silicon.* Physical Review Letters, 1999. 82(19): p. 3823-3826.

13. Bailey, N.P. and J.P. Sethna, *Macroscopic measure of the cohesive length scale: fracture of notected single-crystal silicon.* Physical Review B, 2003. 68: p. 205204.

14. Rueland, E., et al. *Optical u-crack Detection in Combination with Stability Testing for in-line Inspection of Wafers and Cells*. in Proceedings of 20th EU PVSEC 2005. Barcelona.

15. Cotterell, B., et al., *The strength of the silicon die in flip-chip assemblies.* Journal of Electronic Packaging, Transactions of the ASME, 2003. 125(March 2003): p. 114-119.

16. Coletti, G., C.J.J. Tool, and L.J. Geerligs. *Mechanical strength of silicon wafers and its modeling*. in NREL 15th Workshop on Crystalline Silicon Solar Cells and Modules 2005. Vail, Colorado.

17. Grunow, P., et al. *Influence of micro cracks in multi-crystalline silicon solar cells on the reliability of PV modules*. in Proceedings of the 20th EU PVSEC. 2005. Barcelona, Spain.

18. Schneider, A., et al. *Impact of individual process steps on the stability of silicon solar cells studied with a simple mechanical stability tester*. in Conference on PV in Europe, from PV Technology to Energy Solutions. 2002. Rome.

19. Behnken, H., M. Apel, and D. Franke. *Simulation of Mechanical Stress During Bending Tests for Crystalline Wafers*. in 3rd World Conference on Photovoltaic Energy Conversion. 2003. Japan.

20. Sopori, B., P. Sheldon, and P. Rupnowski. *Wafer Breakage Mechanism(s) and a Method for Screening 'Problem Wafers*. in 16th Workshop on Crystalline Silicon Solar Cells and Modules. 2006. Denver, CO.

21. Rueland, E., et al. *u-crack detection and other optical characterisation techniques for in-line inspection of wafers and cells*. in 19th European Solar Energy Conference & Exhibition. 2004. Paris, France.

22. Trupke, T., et al., *Photoluminescence imaging of silicon wafers.* Applied Physics Letters, 2006. 89: p. 044107.

23. Trupke, T., et al. *Fast Photoluminescence Imaging of Silicon Wafers*. in Proceedings of WCPEC-4 2006. Hawaii.

24. Fuyuki, T., et al., *Photographic Surveying of Minority Carrier Diffusion Length in Polycrystalline Silicon Cells by Electroluminescence.* Applied Physics Letters, 2005. 84: p. 262108.

25. Lu, J., et al. *Investigation of Electrical Activity of Dislocation and Grain Boundary in Polycrystalline Float Zone Silicon*. in NCPV and Solar Program Review Meeting. 2003. Denver, Colorado.

26. Rakotoniaina, J.P., et al. *Detection of Cracks in Silicon Wafers and Solar Cells by Lock-in Ultrasound Thermography*. in Proceedings of PV Solar Conference 2004. Paris.

27. Connor, Z.M., et al., *Using scanning acoustic microscopy to study subsurface defects and crack propagation in materials.* JOM, 1998. 50(11).

28. Quate, C.F., A. Atalar, and H.K. Wickramasinghe, *Acoustic microscopy with mechanical scanning - a review.* Proceedings of the IEEE, 1979. 67(8): p. 1092-1114.

29. Wickramasinghe, H.K., *Scanning Acoustic Microscopy: A Review.* Journal of Microscopy, 1983. 129(1): p. 63-73.

30. SONIX, i., *The A,B,C's of Ultrasonics*.

31. Moore, T.M. and C.D. Hartfield. *Trends in nondestructive imagine of IC packages*. in AIP Conference Proceedings. 1998.

32. Hilmersson, C., et al., *Crack Detection in single-crystalline silicon wafers using impact testing.* Applied Acoustics, 2006. Submitted.

33. Belyaev, A., et al., *Crack Detection and Analyses using Resonance Ultrasonic Vibrations in Full-Size Crystalline Silicon Wafers.* Applied Physics Letters, 2006. 88: p. 111907.

34. Byelyayev, A., *Resonance Acoustic Diagnostics in Silicon Wafers* , Master's Thesis in Electrical Engineering. 2002, University of South Florida: Tampa, FL.

35. Scofield, J.H., *A frequency-domain description of a lock-in amplifier.* American Journal of Physics, 1994. 62(2): p. 129-133.

36. Byelyayev, A., *Stress diagnostics and crack detection in full-size silicon wafers using resonance ultraonic vibrations*, Doctoral Dissertation in Electrical Engineering. 2005, University of South Florida: Tampa, FL.

37. Wasmer, K., et al., *Cleavage Fracture of Brittle Semiconductors from the Nanometer to the Centimeter Scale.* Advanced Engineering Materials, 2005. **7**(5): p. 309-317.

38. Belyaev, A., et al., *Resonance ultrasonic vibration diagnostics of elestic stress in full-size silicon wafers.* Semiconductor Science and Technology, 2006. 21: p. 254-260.